Modelling reflected polarized light from close-in giant exoplanet WASP-96b using PolHEx (Polarization of hot exoplanets)

Katy L. Chubb [1,2]★ Daphne M. Stam,[3] Christiane Helling,[2,4]★ Dominic Samra[2] and Ludmila Carone [2]

[1]*Centre for Exoplanet Science, University of St Andrews, North Haugh, St Andrews, KY16 9SS, UK*
[2]*Space Research Institute, Austrian Academy of Sciences, Schmiedlstraße 6, A-8042 Graz, Austria*
[3]*Leiden Observatory, Niels Bohrweg 2, 2333 CA Leiden, Netherlands*
[4]*Fakultät für Mathematik, Physik und Geodäsie, TU Graz, Petersgasse 16, A-8010 Graz, Austria*

ABSTRACT
We present the Polarization of Hot Exoplanets (PolHEx) code for modelling the total flux (F) and degree of linear Polarization (P) of light spectra reflected by close-in, tidally locked exoplanets. We use the output from a global climate model (GCM) combined with a kinetic cloud model of hot Jupiter WASP-96b as a base to investigate effects of atmospheric longitudinal-latitudinal inhomogeneities on these spectra. We model F and P-spectra as functions of wavelength and planet orbital phase for various model atmospheres. We find different materials and sizes of cloud particles to impact the reflected flux F, and particularly the linear Polarization state P. A range of materials are used to form inhomogeneous mixed-material cloud particles (Al_2O_3, Fe_2O_3, Fe_2SiO_4, FeO, Fe, Mg_2SiO_4, MgO, $MgSiO_3$, SiO_2, SiO, TiO_2), with Fe_2O_3, Fe, and FeO the most strongly absorbing species. The cloud particles near the relatively cool morning terminator are expected to have smaller average sizes and a narrower size distribution than those near the warmer evening terminator, which leads to different reflected spectra at the respective orbital phases. We also find differences in the spectra of F and P as functions of orbital phase for irregularly or spherically shaped cloud particles. This work highlights the importance of including Polarization in models and future observations of the reflection spectra of exoplanets.

Key words: scattering – polarization – planets and satellites: atmospheres.

1 INTRODUCTION

The theoretical groundwork for the scattering properties of atmospheric particles derives from prominent works such as Mie (1908); Rayleigh (1918); Chandrasekhar (1950). It was the inclusion of the Polarization state in the modelling of scattered light, however, that was crucial in enabling the identification of cloud types on Venus during the 1970s by Hansen & Hovenier (1974). Via polarimetry they were able to deduce the clouds on Venus were most likely formed from sulphuric acid, with a narrow distribution of particle size and mean radius of $\sim 1\,\mu m$. The method was later utilized further for Venus (e.g. Rossi et al. 2015) and other Solar system planets, such as Mars (Schmude 2008), Jupiter (West & Smith 1991; McLean et al. 2017), Neptune and Uranus (Joos & Schmid 2007), and Saturn (Tomasko & Doose 1984).

Measuring reflection spectra, particularly when including Polarization, is a highly powerful and complementary observation technique to transmission and emission spectroscopy (i.e. observing the light from a star as a function of wavelength during the primary and/or secondary eclipse of a transiting planet) for revealing additional information about transiting exoplanet atmospheres (Millar-

Blanchaer et al. 2018; Muñoz 2018; Fossati et al. 2091). There have been a range of theoretical studies and models of the polarized flux of exoplanet systems, including Seager, Whitney & Sasselov (2000); Bailey, Kedziora-Chudczer & Bott (2018) for close-in giant planets, and Stam (2008); Karalidi & Stam (2012); Fauchez, Rossi & Stam (2017); Rossi & Stam (2017); Groot et al. (2020); Trees & Stam (2022); West et al. (2022) for Earth-like or habitable-zone exoplanets. Observations of Polarization have been proposed in the context of searching for liquid water and biosignatures on Earth-like planets (Berdyugina et al. 2016; Trees & Stam 2019a; Sparks et al. 2021; Vaughan et al. 2023).

By following the orbital phase of a transiting exoplanet, information on the scattered (reflected) light can be determined via the secondary eclipse (when the planet is hidden behind the star) and phase curve mapping (Heng, Morris & Kitzmann 2021; Wong et al. 2021). Although this technique is the same as used for measuring emission spectra, emission and reflection spectra can be disentangled from one another due to the fact they typically dominate across different wavelength regions to one another, with reflection spectroscopy in the visible/near-IR and emission spectroscopy in the IR. There are a number of studies and tools for modelling reflection spectra (Barstow et al. 2014; MacDonald et al. 2018; Batalha et al. 2019; Kawashima & Rugheimer 2019), often with a focus on the overall flux and not considering the Polarization state. Transmission spectra, which can be observed across the whole wavelength region

---

★ E-mail: klc20@st-andrews.ac.uk (KLC); christiane.helling@oeaw.ac.at (CH)

from visible to IR (see, for example, Ahrer et al. (2023); Alderson et al. (2023); Feinstein et al. (2023); Rustamkulov et al. (2023)), do allow some information of spectral cloud features to be inferred (Wakeford & Sing 2015; Mollière et al. 2017; Ormel & Min 2019; Powell et al. 2019; Samra, Helling & Min 2020; Lothringer et al. 2022), in particular at longer wavelengths, around $10\,\mu m$, where there are typically signatures from vibrational modes (Ormel & Min 2019; Bouwman et al. 2023). However, the extent of information to be inferred from these observations is limited. Including the Polarization state in reflection spectroscopy, alternatively, makes the technique particularly sensitive to microphysical cloud properties, such as material and size distribution. Being sensitive to different components of an atmosphere makes polarized reflection spectroscopy a very complementary technique to transmission and emission spectroscopy.

There are a number of ground-based telescopes that can measure the state of Polarization of light, such as HARPSpol (Piskunov et al. 2011), CRIRES + /VLT (Dorn et al. 2023), SPHERE/VLT (de Boer et al. 2020), ZIMPOL/VLT (Gisler et al. 2004), ESPaDOnS (Donati et al. 2006), WIRC + Pol (Tinyanont et al. 2019), PEPSI (Strassmeier et al. 2015), and HIPPI-2 (Bailey et al. 2020). Some of these have been pointed towards exoplanets (Berdyugina et al. 2007, 2011; Bott et al. 2018; Bailey et al. 2021) and Brown Dwarfs (Millar-Blanchaer et al. 2020), however, there is still some discussion over the reliability and interpretation of these exoplanet observations (Bott et al. 2016, 2018). There are already some plans to include polarimeters on future space-based instruments (Takahashi, Matsuo & Itoh 2017), such as LUVOIR/POLLUX (Bouret et al. 2018), and the Nancy Grace Roman Space Telescope (Groff et al. 2021). In order to further motivate the implementation and to facilitate the design of such instruments it is important to have detailed and accurate theoretical models of real systems that are likely to be observed by such instruments, which is the motivation behind the present study.

In this work we present PolHEx, a numerical code for modelling the polarized reflected flux of close-in transiting exoplanet atmospheres. PolHEx is based on the adding-doubling radiative transfer algorithm of de Haan, Bosma & Hovenier (1987), which has been built upon over the years for application to exoplanet atmospheres (Stam et al. 2006; Stam 2008). Versions of the code have been used for modelling for exoplanet atmospheres by many studies, such as Stam et al. (1999a, 2000); Stam, Hovenier & Waters (2004); Stam et al. (2006); Stam (2008); de Kok et al. (2011); Karalidi & Stam (2012); Karalidi, Stam & Hovenier (2012); Karalidi, Stam & Guirado (2013); Fauchez, Rossi & Stam (2017); McLean et al. (2017); Palmer, Rossi & Stam (2017); Rossi & Stam (2017); Trees & Stam (2019b); Groot et al. (2020); Meinke, Stam & Visser (2022); Trees & Stam (2022). There is a publicly available code written in python and fortran called PyMieDap[1] (Rossi, Berzosa-Molina & Stam 2018), which shares much of the functionality and origins with the code in the present study. PolHEx has been specifically tailored for modelling close-in hot exoplanets, which are assumed to be tidally locked. This allows us to directly link longitude/latitude atmospheric variation to orbital phase, and gives a simple way of specifying inhomogeneities in the atmosphere. We use atmospheric climate and kinetic cloud models of hot gas giant exoplanet WASP-96b from Samra et al. (2023) as a base atmosphere to study the impact of inhomogeneous atmospheric composition on reflected flux (F) and degree of linear Polarization (P) using PolHEx. These kinetic cloud models build on a global climate model (GCM) of WASP-96b which was produced

using expeRT/MITgcm (Carone et al. 2020; Baeyens et al. 2021; Schneider et al. 2022).

This paper is structured as follows. Section 2 outlines the relevant theory behind our modelling techniques, with details on the PolHEx code itself given in Section 3. Section 4 summarizes the atmospheric properties of hot gas giant exoplanet WASP-96b which are used in this work, based on the outputs of a GCM and kinetic cloud models. This includes the molecular and cloud composition, pressure–temperature profiles and longitude–latitude grid. Section 5 then details the different theoretical models we have set up based on these atmospheric properties. Here, a number of inhomogeneous (i.e. varying longitude and latitude) and homogeneous (no variation in longitude or latitude) atmospheric models are considered. The results of these models are presented in Section 6, followed by a discussion in Section 7. We present our conclusions in Section 8.

2 THEORY

2.1 Atmospheric scattering

When an oscillating plane electromagnetic (EM) wave emitted from a host star encounters particles (molecular, atomic, cloud) in an orbiting exoplanet's atmosphere, the wave will interact with the charged components of the atmospheric particles. This interaction causes the charged components such as electrons to oscillate with the same frequency as the incident wave, which in turn induces new EM waves that propagate out in all directions from the particle. If a new wave which is propagating in the same direction as the incident beam is out of phase with the incident beam then they will interfere with one another, leading to a change of direction of the incident wave. This process is known as scattering (Mishchenko, Travis & Lacis 2002; Hovenier, Van Der Mee & Domke 2004).

In general, the Polarization state of the stellar EM wave will change during a scattering process. The refractive index $m = n + ik$ of the cloud particles holds information on their scattering properties. This is combined with the wavelength and particle size and shape in order to determine how light is scattered. The real part n of the refractive index represents the phase velocity (rate of propagation) in the material, and the imaginary part k the absorption of incoming radiation by the material.

Each of the atmospheric particles which produce new secondary EM waves due to interaction with the incoming stellar wave will have an impact on the other particles around it. If the number of particles is small the secondary wave contribution can be neglected which leads to the single scattering approximation. If, however, the atmosphere contains many particles, then the scattering of light that has already been scattered by another particle needs to be taken into account. This is known as multiple scattering. PolHEx fully includes multiple scattering effects in it's adding-doubling radiative transfer algorithm (de Haan, Bosma & Hovenier 1987; Stam et al. 2006). In wavelength regions where absorption is high (for example due to a strongly absorbing molecular or atomic transition), multiple scattering effects are reduced. As multiple scattering is a process which tends to reduce the degree of linear Polarization, P, of light in comparison to single scattering, P will generally tend to be higher within strong absorption bands (see Stam et al. 1999b; Stam et al. 2006; Fauchez, Rossi & Stam 2017, and references therein).

2.2 Flux and Polarization state

To describe the flux and Polarization state of the stellar radiation which is scattered towards us, the observer, by the exoplanet's atmo-

---

[1] https://gitlab.com/loic.cg.rossi/pymiedap.git

sphere, we use a Stokes vector (Chandrasekhar [1950](https://); Hovenier & van der Mee [1983](https://); Hovenier, Van Der Mee & Domke [2004](https://); Stam et al. [2006](https://)), as a function of wavelength λ and orbital phase α of the planet orbiting a star (see Section [4.4](https://)):

$$\pi \mathbf{F}(\lambda, \alpha) = \pi \begin{pmatrix} F(\lambda, \alpha) \\ Q(\lambda, \alpha) \\ U(\lambda, \alpha) \\ V(\lambda, \alpha) \end{pmatrix}. \tag{1}$$

The four Stokes parameters forming the vector are defined as follows: F is the total flux, Q and U the linearly polarized fluxes (defined with respect to a reference plane), and V the circularly polarized flux (see Hansen & Travis [1974](https://)). The units of the Stokes parameters are $W\,m^{-2}\,Hz^{-1}$. In our simulations, we will ignore the circular Polarization as the signal is very small compared to the linear Polarization while including it significantly increases computation times (Rossi & Stam [2018](https://)).

The degree of linear Polarization of the radiation is defined as

$$P(\alpha, \lambda) = \frac{\sqrt{Q(\alpha, \lambda)^2 + U(\alpha, \lambda)^2}}{F(\alpha, \lambda)}. \tag{2}$$

We define Q and U when integrated over the planetary disc with respect to the the planetary scattering plane, which is the plane through the centres of the star, the planet, and the observer. We assume that the rotation axis of a transiting planet is perpendicular to this plane (they are tidally locked), and that the observer is facing the system edge-on, that is so the planet's orbital inclination is $90°$. We further assume that the planet is mirror-symmetric about the equator, which means that $U = 0$ when integrated over the planetary disc. This allows the use of an alternative definition of the degree of Polarization P that includes information about the direction of Polarization:

$$P(\alpha, \lambda) = -\frac{Q(\alpha, \lambda)}{F(\alpha, \lambda)}. \tag{3}$$

For positive values of P, the light is polarized perpendicular to the planetary scattering plane (thus perpendicular to the line between the planet and the star), and for negative values of P, the light is polarized parallel to the planetary scattering plane. We chose this convention to ensure P is positive for a clear atmosphere (i.e. only scattering from gaseous species).

In our case, F is the observed flux from the planet, which is composed both of stellar flux reflected by the planet's atmosphere (and surface if there were one), and also of thermal flux from the planet, that is

$$F(\alpha, \lambda) = F_{\text{reflected}}(\alpha, \lambda) + F_{\text{thermal}}(\alpha, \lambda). \tag{4}$$

In the IR wavelength region, the planetary flux is expected to be dominated by emission, whereas in the visible it's expected to be dominated by reflected light. We only consider the degree of Polarization of reflected flux in this study and assume thermal flux is negligible, as we focus on the wavelength region $0.5 - 1\,\mu m$ where the reflected flux will dominate. Therefore, in our case, F in equations (1) – (3) is really just $F_{\text{reflected}}$.

2.3 Scattering by spherical particles

In the models where we assume spherical cloud particles we use Mie theory (Mie [1908](https://)) to compute how radiation is scattered as a function of scattering angle Θ (for forward scattered light, $\Theta = 0°$), using a scattering matrix of the form (see, for example, Hovenier

([1970](https://)); Hovenier, Van Der Mee & Domke ([2004](https://))):

$$\mathbf{F}(\Theta) = \begin{pmatrix} \alpha_1(\Theta) & \beta_1(\Theta) & 0 & 0 \\ \beta_1(\Theta) & \alpha_2(\Theta) & 0 & 0 \\ 0 & 0 & \alpha_3(\Theta) & \beta_2(\Theta) \\ 0 & 0 & -\beta_2(\Theta) & \alpha_4(\Theta) \end{pmatrix}. \tag{5}$$

The first matrix element, $\alpha_1(\Theta)$, is known as the phase function or scattering function. It would be the only element of $\mathbf{F}(\Theta)$ needed if Polarization were to be ignored. The degree of linear Polarization P of light that is singly scattered by the cloud particles is related to the scattering matrix elements of equation (5) by $P = \frac{-\beta_1(\Theta)}{\alpha_1(\Theta)}$.

With PolHEx, a single scattering matrix can be computed for a given particle size distribution. However, we do not use the matrix elements directly in the code's radiative transfer part. Instead we expand them into generalized spherical functions (Kuščer & Ribarič [1959](https://); de Rooij & van der Stap [1984](https://)) and use the coefficients of this expansion. Full details on the expansion of Mie scattering matrices into spherical functions as used in PolHEx can be found in de Rooij & van der Stap ([1984](https://)).

2.4 Scattering by non-spherical particles

Scattering matrices (equivalent to equation (5)) for light that is scattered by non-spherical (e.g. irregularly shaped) particles can be obtained using various methods, such as the Discrete Dipole Approximation (DDA) (Yurkin & Hoekstra [2011](https://)) or the T-matrix method (Mishchenko, Travis & Lacis [2002](https://); Mishchenko et al. [2017](https://)). Although accurate, these methods can take a considerable amount of computational time, especially for particles with a large size parameter x, as defined by

$$x = \frac{2\pi r}{\lambda}, \tag{6}$$

where r is the (equivalent) radius of the particles.

Further, more efficient methods have been developed, such as the Distribution of Hollow Spheres (DHSs) (Min, Hovenier & de Koter [2003](https://), [2005](https://)). In this method, which has been employed by various studies such as Samra, Helling & Min ([2020](https://)), the optical properties of a collection of non-spherical particles with random orientations are approximated by the optical properties of a collection of basic shapes, that is, spherical particles with varying amounts of vacuum inside. It has been shown by Min, Hovenier & de Koter ([2003](https://)) to recreate the measured absorption cross-sections of small crystalline forsterite particles well. We use the publicly available code optool[2] (Dominik, Min & Tazaki [2021](https://)) to compute scattering matrices of irregularly shaped cloud particles. It is derived from codes by Min, Hovenier & de Koter ([2005](https://)) (DHS model for irregular grains) and Tazaki & Tanaka ([2018](https://)) (scattering by fractal dust aggregates). Optool allows a material to be defined, with specified refractive indices, size distribution, wavelength, and degree of irregularity. This degree of irregularity is defined using a parameter called f_{max}, which ranges from 0 for spherical particles to close to 1 for very irregular particles (computationally f_{max} should stay just below 1, e.g. 0.98).

2.5 Rayleigh scattering by molecules

Rayleigh scattering is essentially Mie scattering in the limit of a very small-size parameter x (see equation (6)). Rayleigh scattering will occur due to the small gaseous (molecular and atomic) atmospheric

[2] https://github.com/cdominik/optool

particles. Incident radiation (in this case from the planet's host star) induces a dipole moment in the particle, which is proportional to the incident electric field, with a proportionality constant known as the Polarizability. This Polarizability can be isotropic or non-isotropic. If a particle with $x << 1$ (equation (6)) has isotropic Polarizability then Rayleigh scattering without dePolarization, or isotropic Rayleigh scattering, occurs (Hovenier, Van Der Mee & Domke 2004). If the particle has anisotropic Polarizability, as is the case for H_2 (Kołos & Wolniewicz 2004) for example, then Rayleigh scattering with dePolarization, or anisotropic Rayleigh scattering, occurs. This can be quantified using the dePolarization factor δ, which appears in the equation for the scattering matrix for Rayleigh scattering (Rayleigh 1918; Chandrasekhar 1950; Hansen & Travis 1974):

$$\mathbf{P_m}(\Theta) = \Delta \begin{pmatrix} \frac{3}{4}(1+\cos^2\Theta) & -\frac{3}{4}(\sin^2\Theta) & 0 & 0 \\ -\frac{3}{4}(\sin^2\Theta) & \frac{3}{4}(1+\cos^2\Theta) & 0 & 0 \\ 0 & 0 & \frac{3}{2}\cos\Theta & 0 \\ 0 & 0 & 0 & \Delta'\frac{3}{2}\cos\Theta \end{pmatrix}$$
$$+ (1-\Delta)\begin{pmatrix} 1 & 0 & 0 & 0 \\ 0 & 0 & 0 & 0 \\ 0 & 0 & 0 & 0 \\ 0 & 0 & 0 & 0 \end{pmatrix}, \tag{7}$$

where

$$\Delta = \frac{1-\delta}{1+\frac{\delta}{2}}, \tag{8}$$

$$\Delta' = \frac{1-2\delta}{1-\delta}. \tag{9}$$

The average molecular scattering cross-section σ_m per particle (over all scattering angles Θ) for Rayleigh molecules Hansen & Travis (1974) is:

$$\sigma_m = \frac{8\pi^3}{3} \frac{(n^2-1)^2}{\lambda^4 N^2} \frac{6+3\delta}{6-7\delta}, \tag{10}$$

with $\sigma_m \propto \lambda^{-4}$ indicating that molecular scattering decreases with increasing wavelength. Here, n is the real part of the refractive index of the gas, and N is the number of molecules per unit volume (which depends on the gas temperature, T_{gas}). We use a (wavelength independent) δ of 0.02 for H_2 (Penndorf 1957; Hansen & Travis 1974), as this is the main gaseous component of our model WASP-96b atmosphere.

2.6 Integrated reflection spectra across the planet

For a given orbital phase, the flux vectors from various positions on the planet are integrated over the illuminated part of the planetary disc that is visible by the observer. The Stokes vector of the light that is reflected by the planet and that arrives at the observer can be described by

$$\mathbf{F}(\lambda, \alpha) = \frac{r^2}{d^2} \frac{R^2}{D^2} \frac{1}{4} \mathbf{S}(\lambda, \alpha) \pi \mathbf{B_0}(\lambda), \tag{11}$$

where R is the stellar radius, D the star–planet distance, d is the planet–Earth distance, r is the planet radius, and S the planetary scattering matrix (this describes the light that is reflected by the planet towards the observer) (Stam, Hovenier & Waters 2004). We use cgs units for the distances, and the scattering matrices are unitless. B_0 is the Stokes column vector:

$$\begin{pmatrix} B_0 \\ 0 \\ 0 \\ 0 \end{pmatrix}, \tag{12}$$

with πB_0 the stellar surface flux (units of erg s^{-1} cm^2). The stellar surface flux is assumed to be unpolarized when integrated over the stellar disc (Kemp et al. 1987). Although PolHEx could be adapted for polarized incoming stellar radiation if necessary, we do not in this case because it has been found that most FGK stars have negligible intrinsic Polarization as long as they are inactive (Cotton et al. 2017), and WASP-96 is not known to be particularly active.

In this work, we only compute the planetary scattering matrix, $\mathbf{S}(\lambda, \alpha)$ (Stam, Hovenier & Waters 2004), of our model planets:

$$\mathbf{S}(\lambda,\alpha) = \begin{pmatrix} a_1(\lambda,\alpha) & b_1(\lambda,\alpha) & 0 & 0 \\ b_1(\lambda,\alpha) & a_2(\lambda,\alpha) & 0 & 0 \\ 0 & 0 & a_3(\lambda,\alpha) & b_2(\lambda,\alpha) \\ 0 & 0 & -b_2(\lambda,\alpha) & a_4(\lambda,\alpha) \end{pmatrix}. \tag{13}$$

We set all other terms in equation (11) to 1, and normalize such that F at $\alpha = 0°$ is equal to the geometric albedo; see subsection 2.7. Thus our outputs labelled F are really the $a_1(\lambda, \alpha)$ element of the planetary scattering matrix. These values can be scaled given the parameters of the system; we do not choose to do so in the figures presented here and just look at comparative values, as our main aim is to assess differences between different model atmospheres.

Degree of Polarization P is a relative measure and so does not need to be scaled. We do, however, give some typical scaled values using the WASP-96b system parameters in Appendix A, which we use to comment on the potential detectability of our model planets. In summary, we find a typical range of $\frac{P}{F_{star}}$ (i.e. Polarization as a fraction of the observed stellar flux) of 0.1 – 30 ppm. For reference, the HIPPI-2 instrument can measure a polarized signal with a precision of around 3.5 ppm (Bailey et al. 2020), with higher precisions expected from potential future instruments. This places some of the polarized signals modelled in this work on the edge of the current detectability limits, which may provide guidance for the design of future polarimeters.

Further details on the computation of the planetary scattering matrix can be found in Rossi, Berzosa-Molina & Stam (2018), including the expansion as a Fourier series and the choice of Gaussian abscissae for the integration across the planetary disc, which are also relevant to PolHEx. We find 80 Gaussian abscissae to be sufficiently accurate for our computations.

2.7 Bond and geometric albedo

The Bond albedo, A_B, of a planet is essentially the efficiency with which the planet reflects incoming stellar radiation into all directions. It therefore determines how much energy from stellar radiation is absorbed and available for transport round the planet (see, for example, Chubb & Min (2022)). The geometric albedo, A_G, is defined as the ratio of the reflected flux at $\alpha = 0°$ (i.e. scattering angle $\Theta = 180°$) compared to a Lambertian (isotropically reflecting) flat disc of the same cross-sectional area that comprises the same solid angle in the sky. Unlike A_B, A_G can be larger than 1. For a transiting exoplanet with known radius, A_G can be measured just before the secondary transit. Although both the Bond and the geometric albedo are generally wavelength dependent, they are typically measured and averaged over a band pass (see, for example, Krenn et al. (2023)).

Geometric albedo A_G can be found from the planetary scattering matrix element a_1 as an output of PolHex via

$$A_G = a_1(\Theta = 180°) = a_1(\alpha = 0°). \tag{14}$$

For a model planet with no atmosphere and a Lambertian reflecting surface with an albedo of 1, the planetary scattering matrix element
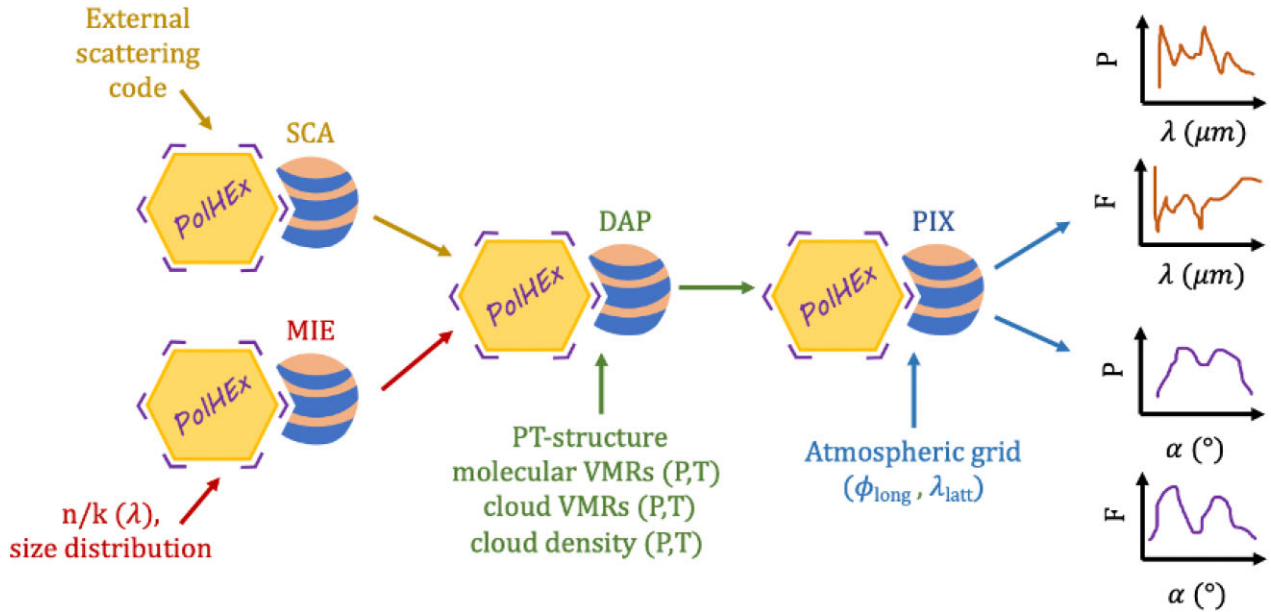
Figure 1. A simplified summary of the PolHEx code setup. Either the MIE routine within PolHEx or an external code can be used for computing the scattering matrices of cloud or aerosol particles. Use of an external code output requires an extra step (SCA) to expand these matrix elements (as functions of scattering angle) into spherical functions, and to format the output for input into the adding-doubling radiative transfer routine (DAP) part of PolHEx. The pressure-dependent atmospheric parameters are setup in DAP for each different atmospheric region on the planet, before combining different regions of the planet together in the PIX component of the code. The outputs from PIX are either F and P as functions of wavelength λ for a fixed orbital phase α, or F and P as functions of α for a fixed λ.

a_1 is given by

$$a_1(\Theta) = \frac{2\pi}{3}(\sin\Theta - \Theta\cos\Theta),\qquad(15)$$

where $\Theta = 180° - \alpha$. There is a factor of 4 difference compared to e.g. Stam et al. (2006), due to our normalization. For a white, Lambertian reflecting planet, at $\Theta = 180°$ or $\alpha = 0°$, $a_1 = A_G = \frac{2}{3}$.

3 THE POLHEX CODE

The PolHEx code is used throughout this study. This code is based on the adding-doubling radiative transfer algorithm of de Haan, Bosma & Hovenier (1987), adapted for and used to model polarized fluxes of light reflected by exoplanets by Stam et al. (2006); Stam (2008). Variations of the code have been used in many studies such as Stam et al. (1999a, 2000); Stam, Hovenier & Waters (2004); Stam et al. (2006); Stam (2008); de Kok et al. (2011); Karalidi & Stam (2012); Karalidi, Stam & Hovenier (2012); Karalidi, Stam & Guirado (2013); Fauchez, Rossi & Stam (2017); McLean et al. (2017); Palmer, Rossi & Stam (2017); Rossi & Stam (2017); Trees & Stam (2019b); Groot et al. (2020); Meinke, Stam & Visser (2022); Trees & Stam (2022). A version of the code was used in a benchmark against the Monte Carlo based radiative transfer code ARTES in Karalidi, Stam & Hovenier (2012). There is a publicly available code written in a combination of python and fortran called PyMieDap[3] (Rossi, Berzosa-Molina & Stam 2018), which shares much of the functionality and origins with PolHEx.

Fig. 1 gives a summary of the structure of PolHEx. Either the MIE routine within PolHEx or an external code can be used to compute single scattering matrices (as in equation (5)) for particle

size distributions of cloud/aerosol particles, resulting in 6 independent matrix elements as functions of the single scattering angle. The scattering matrix elements are expanded in general spherical functions (see subsection 2.3) before being passed on to the adding-doubling radiative transfer (DAP) part of PolHEx. If an external code is used to compute the single scattering matrix elements of the cloud/aerosol particles, then an extra step is required for their expansion (this is done by the SCA component of the code, as labelled in Fig. 1). The atmosphere is also built as input to DAP, as described in Section 4 for our WASP-96b model atmospheres. Molecular absorption and scattering are both included here. The pressure-dependent atmospheric parameters are set up in DAP for a number of atmospheric layers. The geometry of the system is set up in this part of the code, including the atmospheric composition as a function of longitude and latitude.

The output of DAP entails the reflection of unpolarized incident light for a range of local illumination and viewing angles for a given planetary model atmosphere. The matrix elements which describe this local reflection of the planet (in our case due to the atmosphere only) are expanded as a Fourier series, the coefficients of which can be read into the PIX part of PolHEx, for integrating the locally reflected light across the illuminated and visible part of the planetary disc for a given phase angle α.

The planetary disc can be horizontally inhomogeneous with different local atmospheres on different parts of the disc. In order to perform the integration across the inhomogeneous planetary disc, different Fourier coefficients are computed for the different regions on the planet and these different coefficients are then read and used for the integration. With an increasing number of different regions, the computation time also increases, so some compromise needs to be made between the degree of complexity regarding the inhomogeneities and computational speed.

[3]https://gitlab.com/loic.cg.rossi/pymiedap.git
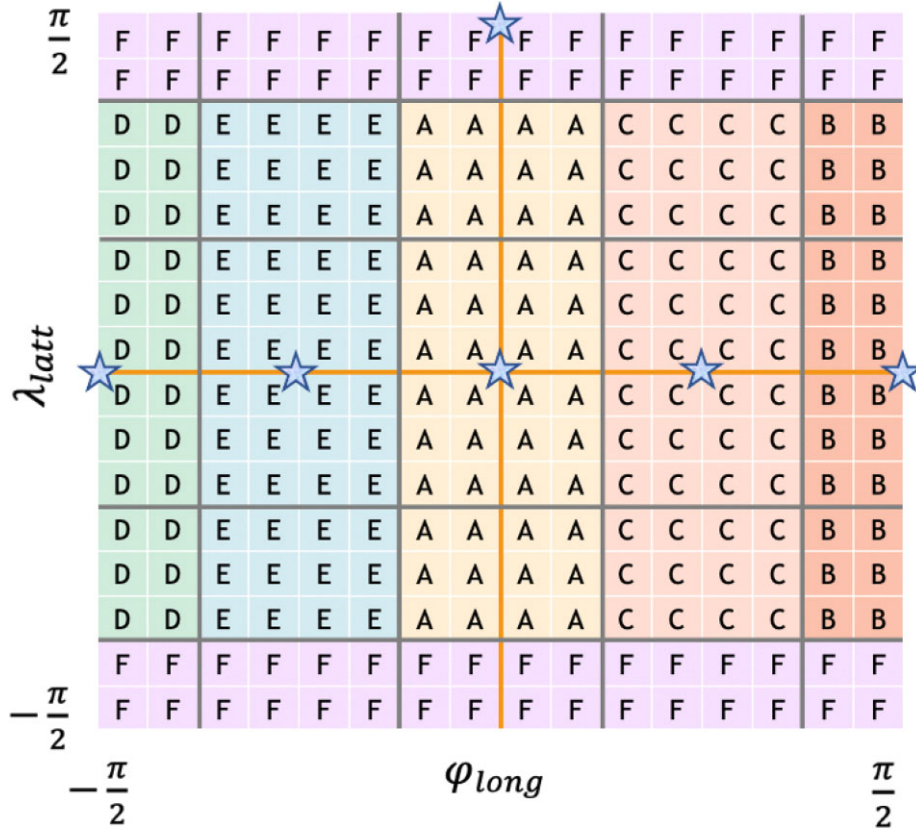
Figure 2. An illustration of the division of the dayside of WASP-96b into different local model atmospheres. The letter denoting the composition is linked to the output of StaticWeather (Samra et al. 2023) for WASP-96b for the following longitude (ϕ_{long}) / latitude (λ_{latt}) points: A = 0° / 0°, B = 90° / 0°, C = 45° / 0°, D = –90° / 0°, E = –45° / 0°, F = 0° / 86°. The blue stars indicate the locations of these longitude / latitude points. A larger grid (64 × 64) is used in this work but with the same proportions covered by each atmosphere type.

PolHEx computes planet reflection for α from 0° to 360° in steps of 10°, with 0° being when the planet is directly behind the star, 90° when the morning terminator is turned towards the observer, 180° when the planet is in front of the star (mid-transit), 270° when the evening terminator is turned towards the observer, and 360° when the planet is again behind the star. The outputs of PolHEx, as labelled in Fig. 1, are either *F* and *P* as functions of wavelength λ for a fixed value of α, or *F* and *P* as functions of α for a fixed value of λ.

4 THE ATMOSPHERE OF WASP-96B

WASP-96b is a hot gaseous exoplanet with a mass of $0.48 \pm 0.03 \, \text{M}_{\text{Jup}}$, and a mean radius of $1.2 \pm 0.06 \, \text{R}_{\text{Jup}}$. It orbits close to its host star, with a semimajor axis of 0.045 au and an orbital period of 3.4 d (Hellier et al. 2014). The transmission spectra of WASP-96b have been observed and its atmosphere characterized using the Very Large Telescope (VLT), *Hubble Space Telescope* (*HST*), and the *Spitzer Space Telescope* (Nikolov et al. 2018, 2022), and more recently with JWST's NIRISS/SOSS instrument (Radica et al. 2023; Taylor et al. 2023).

Our base planetary atmosphere setup is derived from the output of a global circulation model (GCM) of WASP-96b which was produced using expeRT/MITgcm (Carone et al. 2020; Baeyens et al. 2021; Schneider et al. 2022) and combined with a kinetic cloud modelling routine (Helling et al. 2019, 2021) in Samra et al.

(2023). We explore how varying certain parameters, such as the materials forming cloud particles, impacts the reflected flux and Polarization of the planet. We utilize the output provided as a result of Samra et al. (2023) for 6 different longitude and latitude dependent atmospheric regions, which we label A...F, as shown in Fig. 2.

For each atmospheric region A...F, we build an atmosphere with 44 plane-parallel atmospheric layers, with the pressure and temperatures for each taken from Samra et al. (2023) and shown in Fig. 3. We assign the volume mixing ratio (VMR) of molecules, material volume fractions of the clouds, and optical depth of clouds for each region as described further. There is no clearly defined surface on hot gaseous exoplanets, so we use atmospheric layers down to a pressure of 6 bar, and describe the deeper layers as a black surface, that is, all the light emerging from the bottom of the lowest layer (at 6 bar) is absorbed.

4.1 Gaseous composition

The molecular volume concentrations $\frac{n_i}{n_{\text{tot}}}$ (number of molecules of a given species per unit volume $\frac{n_i}{n_{\text{tot}}}$ divided by the total number of molecules in that volume) at each of the 6 atmospheric regions A...F in Fig. 2 are shown in Appendix Fig. B3. For simplicity, and because most of the molecular VMRS are very similar between different regions, we only use the two terminator regions (B and D) for modelling the molecular composition, see Fig. 4. The model atmosphere contains only the most abundant
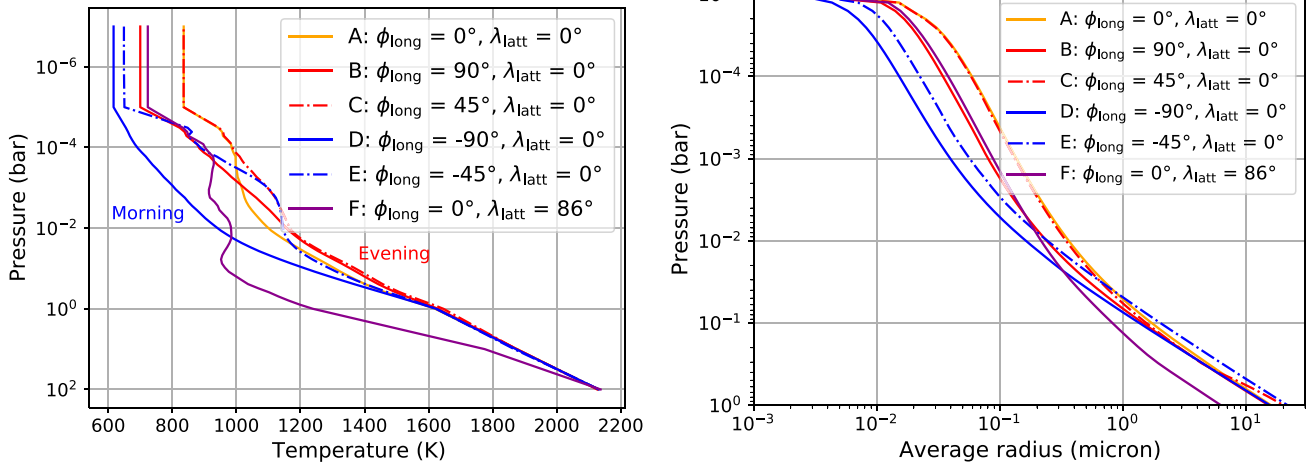
Figure 3. Left: Pressure–temperature profiles for the atmospheric regions A to F shown in Fig. 2. Right: Average particle radii for the same regions.
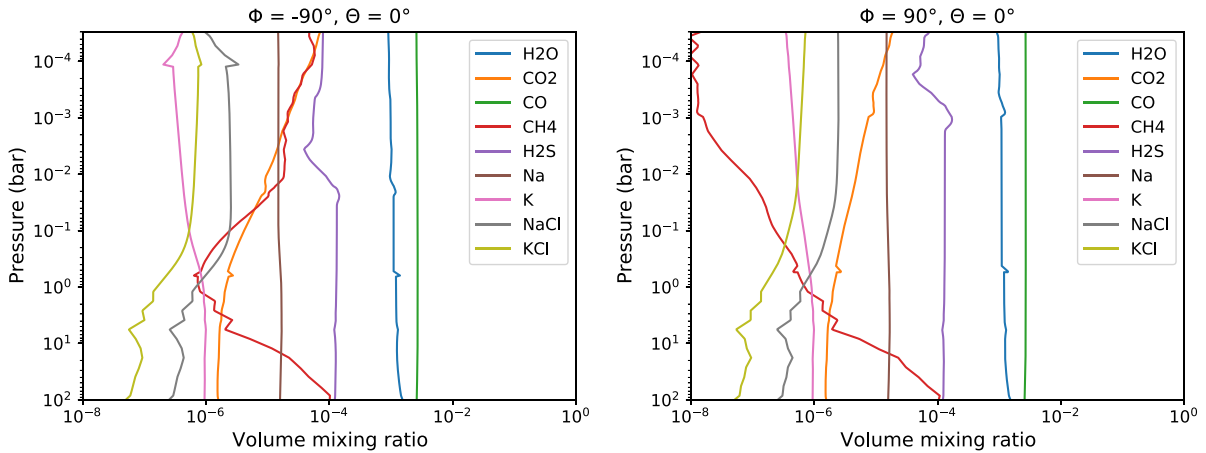
Figure 4. Molecular and atomic concentrations n_i/n_{tot} for WASP-96b atmospheric models. Left: at $\phi_{long} = -90°$, $\lambda_{latt} = 0°$ (cooler morning terminator), and right: $\phi_{long} = 90°$, $\lambda_{latt} = 0°$ (warmer morning terminator).

species (H$_2$O (Polyansky et al. 2018), CO (Li et al. 2015), H$_2$S (Azzam et al. 2016), CH$_4$ (Yurchenko et al. 2017), Na (Kramida, Ralchenko & Reader 2013; Allard et al. 2019), and K (Kramida, Ralchenko & Reader 2013; Allard, Spiegelman & Kielkopf 2016)). The remainder of the atmosphere is comprised of H$_2$ and He, in solar abundances.

We use absorption cross-sections (in cm^2/molecule) computed using ExoCross (Yurchenko, Sergei N., Al-Refaie, Ahmed F. & Tennyson, Jonathan 2018) as part of the ExoMolOP data base (Chubb et al. 2021), with the line list for each as specified above. In general, we do not expect to see spectral features from these species at abundances below around 1×10^{-6} (Gasman, Min & Chubb 2022), however, we include the atoms Na and K because of their very strong resonance doublet features. Such features have been observed in the atmosphere of WASP-96b using the VLT (Nikolov et al. 2018). We bin the combined cross-sections which include all these species down to a small number of wavelengths (58), ensuring sufficient sampling around the prominent spectral features. These absorption features are most apparent in our clear (i.e. cloud-free) atmospheric models, but are also important in our cloudy models in order to explore the scattering behaviour within and outside the regions of the absorption features.

4.2 Cloud composition

Samra et al. (2023) predict a variety of different species to form clouds in WASP-96b-like atmospheres. Building an inhomogeneous atmosphere of WASP-96b allows us to investigate

   (i) different cloud compositions,
   (ii) different cloud particle sizes and distributions, and
   (iii) clouds at different layers of the atmosphere

We then explore these further using model homogeneous atmospheres, largely based on either atmospheric region B (around the evening terminator) or D (around the morning terminator). We set up an atmosphere using PolHEx, which allows for a user-defined number of atmospheric layers, each with its own pressure, temperature, gaseous abundance, and cloud layer. For the cloud layer at each pressure level, expansion coefficients of the respective single scattering matrix are read in, with clouds composed of different materials already pre-mixed, as explained in subsection 4.2.2. The scattering properties of the cloud particles can either be computed using the internal PolHEx-MIE computation, which uses Mie theory and therefore assumes spherical particles, or from an external source.

Table 1. Sources used for the real (n) and imaginary (k) parts of the refractive indices of the species that form cloud particles in this work. Average values across the wavelength range we consider ($0.5 - 1\,\mu m$) are given. All species are in solid phase.

Species	Name	n	k	Source
Al_2O_3 (crystalline)	Corundum	1.76	0	Palik (2012)
Fe_2O_3 (solid)	Hematite	2.79	0.22	Triaud (2005)[a]
Fe_2SiO_4 (crystalline)	Fayalite	1.85	1.16×10^{-3}	Unpublished[b]
FeO (amorphous)	Wustite	2.43	0.55	Henning et al. (1995)
Fe (metallic)	Iron	2.66	3.64	Palik (2012)
Mg_2SiO_4 (amorphous)	Forsterite	1.61	1.22×10^{-4}	Jäger et al. (2003)
MgO (cubic)	Magnesium oxide	1.74	6.76×10^{-8}	Palik (2012)
$MgSiO_3$ (amorphous)	Enstatite	1.57	2.99×10^{-5}	Dorschner et al. (1995)
SiO_2 (crystalline)	Quartz	1.54	0	Palik (2012)
SiO (non-crystalline)	Silicon oxide	1.93	6.61×10^{-3}	Palik (2012)
TiO_2 (rutile)	Rutile	2.54	2.40×10^{-4}	Zeidler et al. (2011)

Notes.[a]- Downloaded via the Aerosol Refractive Index Archive (ARIA) at http://eodg.atm.ox.ac.uk/ARIA/
[b]- Accessed via the Data base of Optical Constants for Cosmic Dust at https://www.astro.uni-jena.de/Laboratory/OCDB/crsilicates.html

We use the optool code[4] (Dominik, Min & Tazaki 2021) (see subsection 2.4) for exploring the impact of irregularly shaped rather than spherical particles in the atmosphere. We check for consistency with the MIE computations of PolHEx for spherical particles for each set of refractive indices and size distributions, and find identical results.

4.2.1 Materials used for clouds

Table 1 gives a summary of the different materials used to form the clouds in this work, along with the references for their refractive indices as a function of wavelength. The real n and imaginary k parts of the refractive indices (sometimes known as optical constants) as functions of wavelength can be seen in Fig. 5. It is worth noting that the Fe-bearing species Fe, FeO, Fe_2O_3 have the highest values of k, which signifies they are highly absorbing. The same species, along with TiO_2 have relatively high values of n, which indicates a high phase velocity (rate of propagation) which impacts scattering. We note that some typical spectral features that are driven by the imaginary component of the refractive index occur at longer wavelengths than those shown here.

There are a number of data bases which can be used to search for the wavelength-dependent refractive indices of materials which are used to form the clouds. For example, the Data base of Optical Constants for Cosmic Dust[5] (Mutschke et al. 2023), and the ARIA[6] (Grainger et al. 2023) were both used in the present work (see Table 1). The optical properties of potential condensates in exoplanetary atmospheres, including many of those included in this work, have also been compiled and made publicly available in the github associated with various works, such as Kitzmann & Heng (2017).

4.2.2 Mixing materials to form clouds using effective medium theory

In realistic scenarios, and as demonstrated in Samra et al. (2023) for WASP-96b, we expect clouds to be formed not of just one single material, but of several different species. In order to model clouds formed of different materials, we use effective medium theory

to compute the complex refractive indices which result from the different materials combined (Mishchenko, Dlugach & Liu 2016). Each material has it's own real n and imaginary k part of the refractive index, which varies by wavelength, as illustrated by Fig. 5. We take into account the material volume fractions of different cloud materials for different longitude, latitude, and pressure layer (as illustrated in Fig. 6; here, the volume fractions are only as proportions of the total cloud composition and do not take molecular abundances into account), along with the refractive index for each material as a function of wavelength, in order to get a mixed refractive index as a function of wavelength and pressure layer for each atmospheric region (Appendix Fig. B1). We mix all species given in Fig. 6 together, taking their relative material volume fractions into account. An example of how these species contribute to the mixed-material refractive indices of Appendix Fig. B1 is illustrated in Appendix Fig. B2, which shows the real part of the mixed-material refractive index n when including selected materials for atmospheric region B (evening terminator) at 0.1 bar and 1×10^{-4} bar. It can be seen that n when including all materials is identical to n with only the four most abundant species in the left panel (0.1 bar), with Al_2O_3 only acting to reduce the value of n at the higher wavelengths. The right panel (1×10^{-4} bar), however, demonstrates that a larger number of materials are contributing to n in the upper atmosphere. The number of species which contribute to the mixed-material refractive index is therefore dependent on the atmospheric layer and region, and only including a small number of the most abundant species rather than all materials will have an impact on the resulting modelled spectra. The materials used to form all cloud particles are based on the assumed elements available in the exoplanet's atmosphere, along with the local thermodynamic conditions. 132 gas–surface growth reactions are taken into account for the mixed-material cloud particle formation (Helling 2022; Helling et al. 2023).

We use the Bruggeman mixing rule (Bruggeman 1935), as was used, for example, in recent works such as Samra (2022); Samra, Helling & Birnstiel (2022):

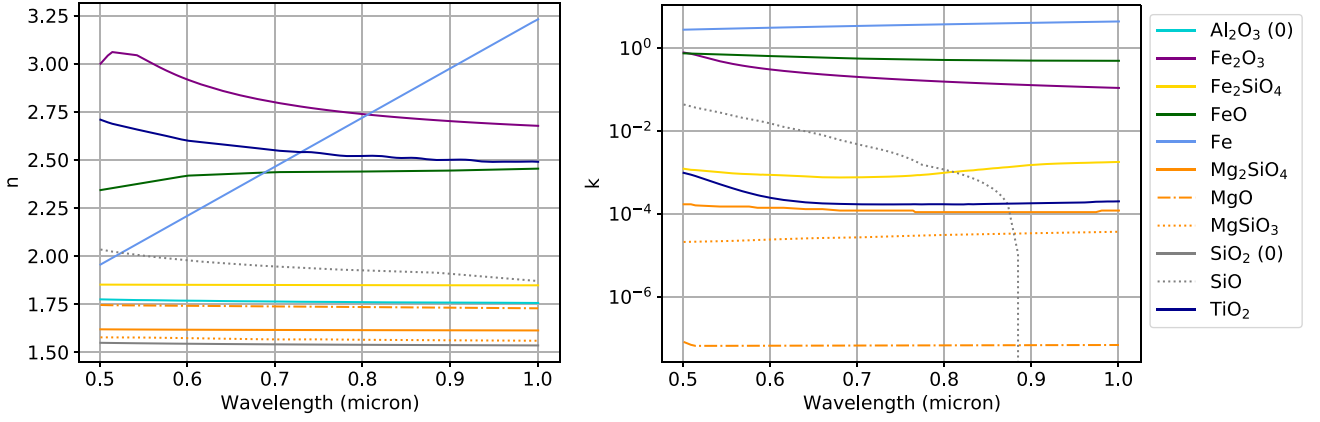$$\sum_s \frac{V_s}{V_{tot}} \frac{\epsilon_s - \epsilon_{eff}}{\epsilon_s + 2\epsilon_{eff}} = 0. \tag{16}$$

Here, ϵ_s is the dielectric constant of each individual condensate material which makes up the inhomogeneous cloud particles. ϵ_s is related to the refractive index by: $\epsilon_s = (n + ik)^2$. We solve equation (16) iteratively using Mathematica (Wolfram 2022) to get the combined (or effective) dielectric constant ϵ_{eff}, which can be split into real n_{eff} and imaginary k_{eff} parts. We compute these effective

---

[4] https://github.com/cdominik/optool
[5] https://www.astro.uni-jena.de/Laboratory/OCDB/
[6] http://eodg.atm.ox.ac.uk/ARIA/

Figure 5. The real (left) and imaginary (right) parts n and k of the refractive index for species used in this work (for references, see Table 1). The real part of the refractive index indicates the phase velocity (rate of propagation), which relates to scattering, whereas the imaginary part relates to the material's absorption properties. The (0) in the legend refers to the imaginary part k being zero across all wavelengths shown for that species.
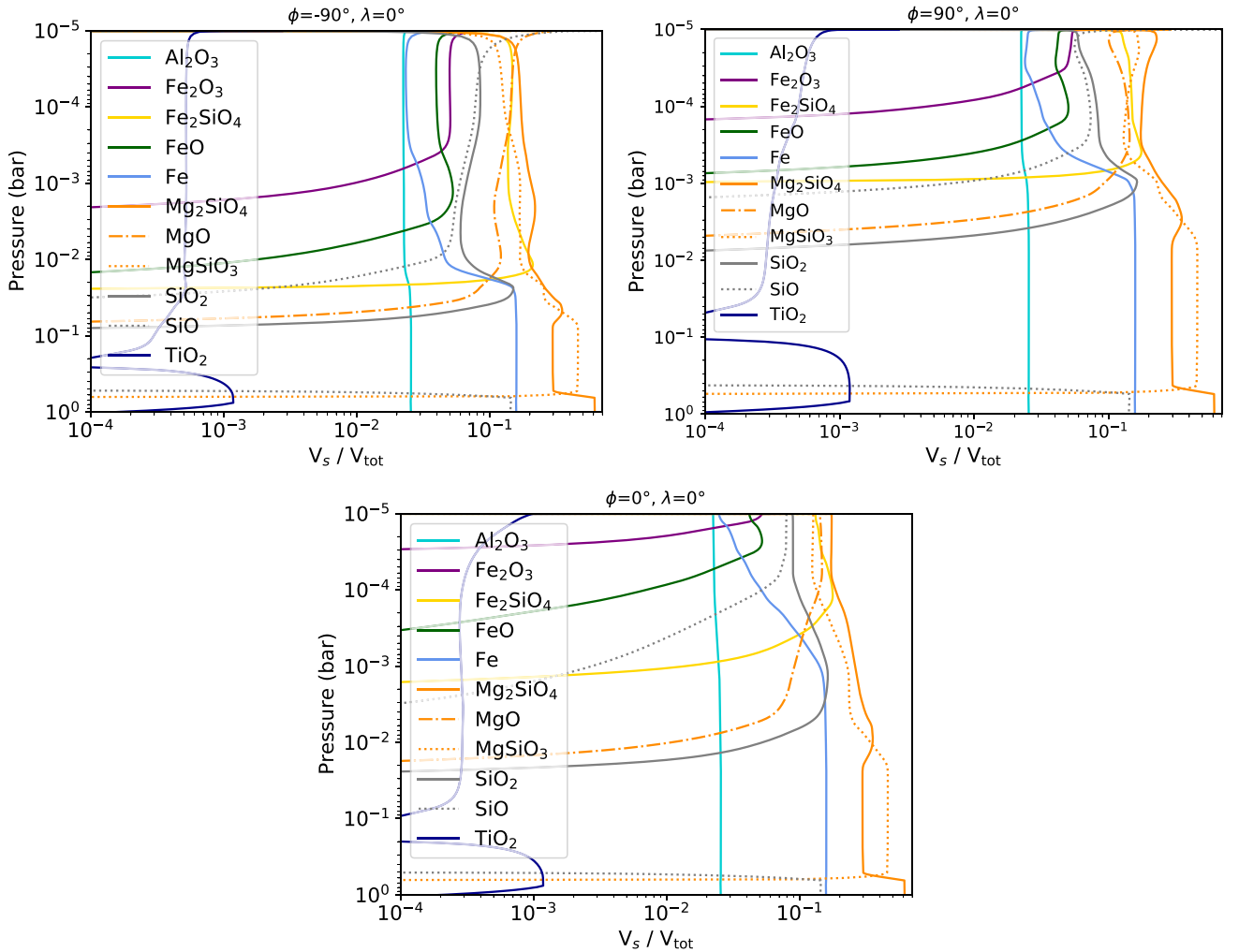
Figure 6. Material volume fractions V_s / V_{tot} of the different materials forming the mixed-material cloud particles. Upper left: for $\phi_{long} = -90°$, $\lambda_{latt} = 0°$ (cooler morning terminator); upper right: $\phi_{long} = 90°$, $\lambda_{latt} = 0°$ (warmer evening terminator); and lower centre: $\phi_{long} = 0°$, $\lambda_{latt} = 0°$ (the substellar point).
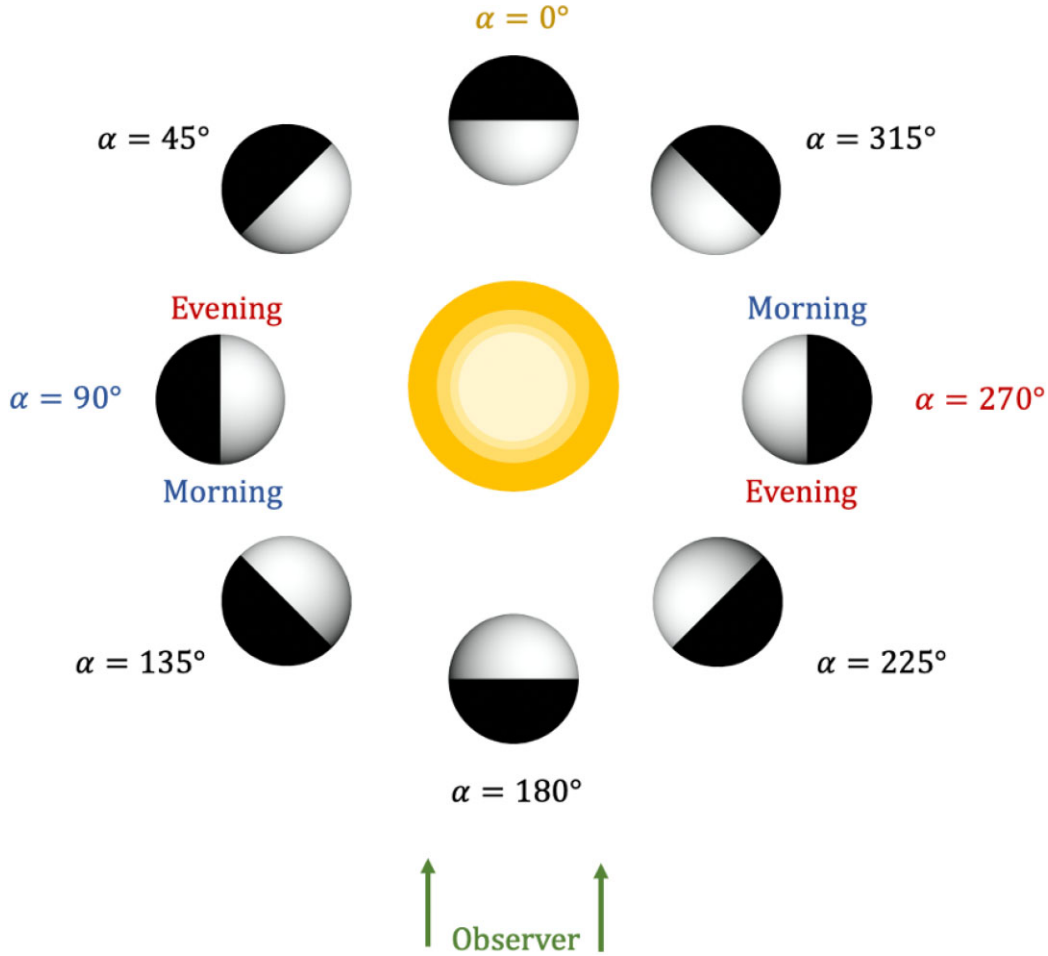
Figure 7. An illustration of how we define phase angle α, with a face-down view of the planet-star system. We assume tidally locked planets, so the rotation period of the planet on its axis is the same as the orbital period, both in the anticlockwise direction in this diagram. The direction of observation is indicated, with the cooler morning terminator in view at $\alpha = 90°$ and the warmer evening terminator in view at $\alpha = 270°$.

refractive indices as a function of longitude, latitude, pressure layer, and wavelength, and use them as input into our PolHex WASP-96b models.

4.3 Optical depth of clouds

Strong spectral features of Na and K have been observed in the transmission spectra of WASP-96b using the VLT, *Hubble Space Telescope* (*HST*) and the *Spitzer Space Telescope* (Nikolov et al. 2018, 2022). The conclusion of Nikolov et al. (2018) was that the atmosphere must be cloud-free in order for the line-wings of the atomic absorption features to be visible. The GCM and kinetic cloud models of Samra et al. (2023), however, find that it would be very unlikely for WASP-96b to be cloud free. Samra et al. (2023) therefore explored how their models could better match up with the observations, with one of the processes being a reduced atmospheric vertical mixing, which would cause clouds to settle deeper in the atmosphere than originally predicted. In this work we choose the lower altitude cloud layer in our inhomogeneous model atmosphere models, in order to be more consistent with the observations of Nikolov et al. (2018). We do also demonstrate an inhomogeneous model where we place the cloud layer higher up in the atmosphere (to become optically thick at 1×10^{-4} bar), as a comparison (see Table 2 for a summary of the different models computed in

this study).

We assume that within each atmospheric layer the number density N_{cloud} of the materials (both molecules/atoms and clouds) within remains constant. This means the optical depth τ of a given layer of length l due to clouds composed of a variety of materials with combined extinction coefficient k_{ext} can be deduced by

$$\tau = k_{\mathrm{ext}} N_{\mathrm{cloud}} l. \tag{17}$$

We use cgs units in our code, with l in cm, N_{cloud} in $\frac{g}{cm^3}$, and k_{ext} in $\frac{cm^2}{g}$. Optical depth τ is unitless. Extinction coefficient k_{ext} is sometimes called attenuation cross-section σ_{cloud}. k_{ext} is the sum of the scattering k_{scat} and absorption k_{abs} cross-sections:

$$k_{\mathrm{ext}} = k_{\mathrm{scat}} + k_{\mathrm{abs}} \tag{18}$$

The ssa can be found from these:

$$\mathrm{ssa} = \frac{k_{\mathrm{scat}}}{k_{\mathrm{ext}}} \tag{19}$$

4.3.1 Particle size distribution

Although various size distributions can be used in the Mie computations within PolHex (Hansen & Travis 1974; de Rooij & van der Stap 1984), we choose to use a simple Gaussian distribution

Table 2. A summary of the different model atmospheres computed in this study. Note that $\alpha = 90°$ and $\alpha = 270°$ are identical in the cases of (longitudinally/latitudinally) homogeneous atmospheres, so only $\alpha = 90°$ is shown in those cases.

Description	Associated figure
Inhomogeneous model atmospheres: *F* and *P* as a function of wavelength for $\alpha = 90°$ and $\alpha = 270°$	
WASP-96b setup including atmosphere types A...F, with and without clouds, and varying optical depth	Fig. 9
WASP-96b setup including atmosphere types A...F, for irregularly shaped particles above 0.01 bar	Fig. 9
Inhomogeneous model atmospheres: *F* and *P* as a function of orbital phase for selected wavelengths	
WASP-96b setup including atmosphere types A...F with clouds of mixed composition	Fig. 10
WASP-96b setup including atmosphere types A...F with no clouds (clear)	Fig. 11
WASP-96b setup including atmosphere types A...F, for irregularly shaped particles above 0.01 bar	Fig. 12
Homogeneous model atmospheres: *F* and *P* as a function of wavelength for $\alpha = 90°$	
A series of 6 model atmospheres, of types A...F, each with mixed species used to form clouds	Fig. 13
A series of models of atmosphere type B, each with one single species used to form the clouds	Fig. 14
A series of models of atmosphere type D, each with one single species used to form the clouds	Fig. 15
A series of 5 model atmospheres of type B, with varying irregularity of clouds particles	Fig. 17
11 models of type B, with one single species used to form clouds and $0.25/2.5 \times 10^{-4}$ μm size distribution	Fig. 18
11 models of type B, with one single species used to form clouds and 0.1/0.01 μm size distribution	Fig. 19
Models of type B, each with Mg_2SiO_4 only used to form clouds and various Gaussian size distributions	Fig. 20
Homogeneous model atmospheres: *F* and *P* as a function of orbital phase for selected wavelengths	
Mixed cloud composition type B, compared to models with one single species used to form the clouds	Appendix Fig. B4/B5

(Samra, Helling & Min 2020) for the local size distribution of cloud particles in each atmospheric layer and region. See subsection 7.3 for a discussion on different particle size distributions. The average particle size r_g as a function of pressure for each atmospheric region A...F are illustrated in Fig. 3. We assume a Gaussian distribution standard deviation around each of these average particle sizes which is an order of magnitude less than each of the average particle sizes assumed. It can be seen from Fig. 3 that the evening terminator region (B) is warmer than the morning terminator region (D). This generally implies a smaller average particle size for the cooler morning terminator than for the warmer evening terminator.

4.4 Geometry of WASP-96b's transit

PolHEx is setup with the hot exoplanets assumed to be tidally locked to their host star. This means that the same face of the planet is always facing the star. This simplifies the part of the planet visible to the observer, with the convention of phase = 0° for the dayside of the planet facing the observer and phase = 180° for the nightside of the planet facing the observer. Phases of 90° and 270° correspond to the morning and evening terminators directly facing the observer, respectively. An illustration of this and a definition of how the phase angles are defined is given in Fig. 7, which gives a face-down perspective of the geometry. Only the dayside part of the planet ($-\frac{\pi}{2} \geq \phi_{long} \leq \frac{\pi}{2}$, $-\frac{\pi}{2} \geq \lambda_{latt} \leq \frac{\pi}{2}$) will give non-zero reflected stokes vectors. Under our assumption of a tidally locked planet we can therefore assign atmospheric types based on regions of longitude and latitude, and these definitions will hold for all phase angles. The illuminated part of the planet which is visible to an observer of course changes as a function of orbital phase, as illustrated in Fig. 8.

5 DIFFERENT ATMOSPHERIC SETUPS

The atmosphere is divided into $nlatt = 64$ longitude ϕ_{long} and $nlong = 64$ latitude λ_{latt} points. Each of these grid points is assigned an atmospheric type, computed from the radiative transfer adding-doubling part of the code. For simplicity we have divided WASP-96b up into six atmospheric regions A...F, as described in Section 4 and illustrated in Fig. 2. The locally reflected Stokes vectors are computed for each longitude–latitude grid point and then integrated over the

visible and illuminated part of the planetary disc, in order to get the total reflected stokes parameters for a given orbital phase (as in Figs 7 and 8). Enough latitude and longitude grid points need to be used such that the stokes vector does not vary significantly between adjacent grid points. The method of assigning grid points ensures that the planet is well sampled around the terminator and polar regions. An adequate number of grid points to converge was found to be 64×64.

Each model atmosphere consists of 44 layers. The following parameters (see Section 4 for details) are varied for each model atmosphere type (region in longitude and latitude space) and atmospheric layer (altitude or pressure layers):

(i) gas temperature (K) as a function of gas pressure (bar)

(ii) molecular/atomic number densities (cm^{-3}) as a function of pressure

(iii) size distribution of cloud particles for that given pressure layer*

(iv) complex refractive index as a function of pressure, computed using effective medium theory to mix different materials together*

(v) the wavelength-dependent optical depth of clouds as a function of pressure layer

*For these cloud parameters we do not compute a different set for every one of the 44 layers, but group them together into sub-groups of similar composition and size distribution (cloud layers). This is largely due to the computational load of including separate scattering matrices into every layer for the radiative transfer part of the code. We use five different cloud layers (distributed evenly in log-pressure) to capture the variations in size distributions and compositions throughout the atmospheres. We note that the total number of atmospheric layers does not significantly affect our model results, but the reflected flux and Polarization are sensitive to the minimum and maximum pressures for each cloud layer because those pressures determine the ratio of gas molecules versus cloud particles in each layer.

The different model setups that we compute in this work are summarized in Table 2, along with the figure(s) which demonstrate the results of these models. In general we produce figures for the total flux $F(\lambda, \alpha)$ and degree of linear Polarization $P(\lambda, \alpha)$ for model atmospheres as either a function of wavelength (between $0.5 - 1$ μm)
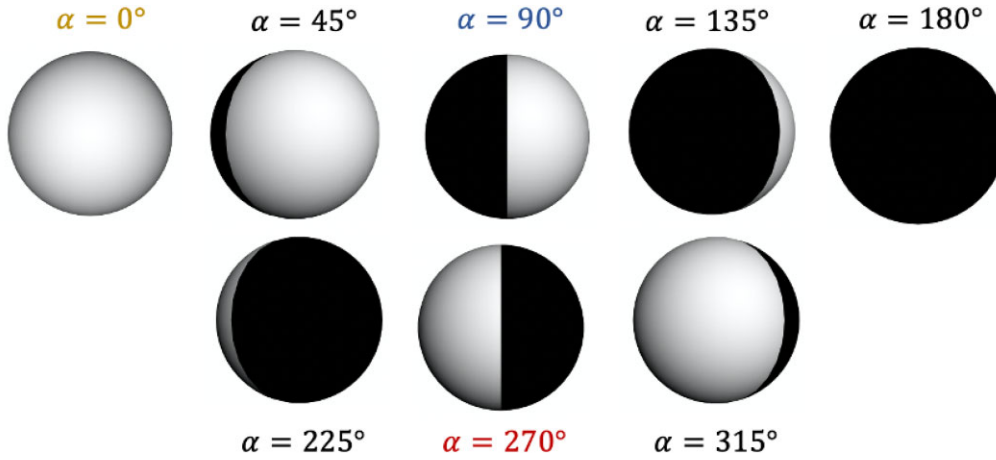
Figure 8. An illustration of the planetary disc as seen by the observer (if it could be resolved) as a function of α. The cooler morning terminator at $\alpha = 90°$ and the warmer evening terminator at $\alpha = 270°$ are highlighted as the phases we focus on in this paper.

for $\alpha = 90°$ or $\alpha = 270°$, or as a function of orbital phase (between $0 - 360°$) for a selection of wavelengths. Here, we use the term homogeneous in terms of longitude and latitude; there is variation with altitude in all models we call homogeneous.

6 RESULTS FOR WASP-96B

6.1 Inhomogeneous model atmospheres: *F* and *P* as a function of wavelength for $\alpha = 90°$ and $\alpha = 270°$

Fig. 9 gives F and P as a function of wavelength for different inhomogeneous model atmospheres (i.e. those which vary as a function of longitude ϕ_{long} and latitude λ_{latt}), at orbital phases of $90°$ and $270°$. The full inhomogeneous atmosphere (orange and turquoise dashed lines) is with a cloud layer that becomes optically thick at 1×10^{-2} bar (see discussion at the start of Section 4). We also include models where the cloud layer becomes optically thick higher in the atmosphere, at 1×10^{-4} bar. The flux as a function of wavelength is relatively low in both scenarios, but the degree of linear Polarization is markedly different. We also show completely clear (no cloud) models in Fig. 9, which are nearly identical for both F and P at phase $90°$ and $270°$. This illustrates that it is the cloud particles (in particular their refractive properties and size distributions) which are causing the differences in reflected flux and degree of Polarization between the different model atmospheres. We explore further why these differences occur, using model homogeneous models and scattering properties of different species, in subsections 6.3 and 6.4.

Similar to the models of Jupiter-like exoplanets in Stam, Hovenier & Waters (2004), the clear atmosphere in Fig. 9 has a general trend of decreasing F with λ, due to a decrease in the molecular scattering optical thickness with λ. P has a corresponding general increase with λ, due to less multiple scattering taking place at longer wavelengths because of the lower molecular scattering cross-section. Multiple scattering typically lowers the degree of Polarization P for reflected light. The regions of increased molecular and atomic absorption can clearly be seen in the clear spectra of Fig. 9 (left). The most prominent absorption features occur around $0.6\,\mu$m and just under $0.8\,\mu$m, due to strong resonance transition doublets of Na and K (Allard, Spiegelman & Kielkopf 2016; Allard et al. 2019). In these regions the strong absorption also causes less multiple scattering to take place. This absorption thus leads to low F and high P.

In the models described so far, it is assumed that all cloud particles are spherical, with scattering properties computed using Mie theory. We also compare to a full inhomogeneous atmosphere with the same properties as in the dashed lines of Fig. 9, but with irregularly shaped instead of spherical particles used for modelling the particles at pressure layers of 0.01 bar and above, for the atmosphere where the clouds become optically thick at 1×10^{-2} bar. We use the optool code[7] (Dominik, Min & Tazaki 2021) (see subsection 2.4) for modelling the scattering properties of the irregularly shaped particles. The value of f_{max} indicates the irregularity of the particle, with 0 a sphere (red) and higher values being more irregular. If the dotted (irregular particles) and dashed (spherical particles) lines of Fig. 9 are compared, the difference between inhomogeneous atmospheres with spherical and very irregular particles ($f_{max} = 0.8$) can be seen, particularly for the degree of linear Polarization P. The irregularly shaped particles generally lead to a higher F and P than the spherical particles, although this behaviour does not hold for the higher wavelengths of the morning terminator models for both F and P.

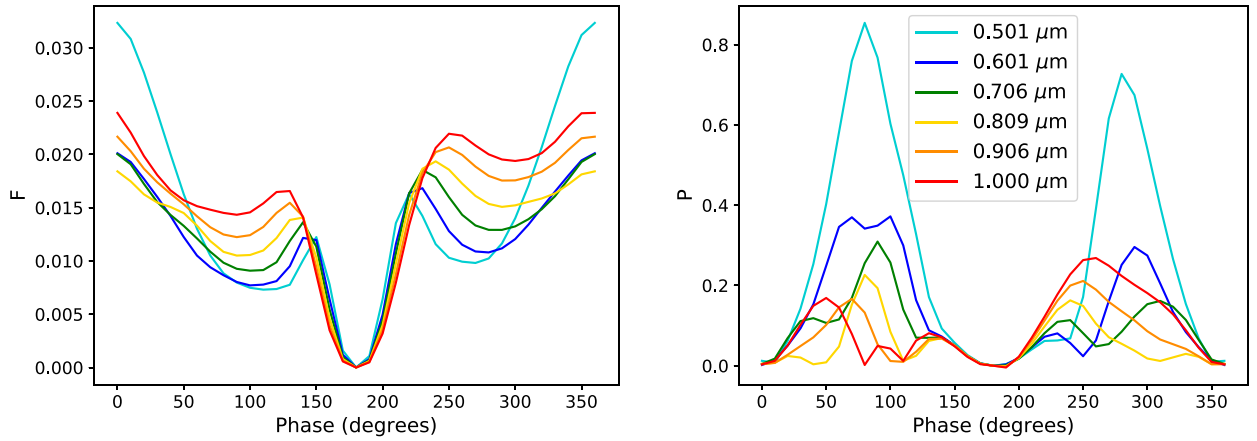### 6.2 Inhomogeneous model atmospheres: *F* and *P* as a function of orbital phase for selected wavelengths

In Fig. 10, we plot F (left) and P (right) as a function of orbital phase for selected wavelengths between 0.5 and 1 μm for the full inhomogeneous model atmosphere (with clouds becoming optically thick at 1×10^{-2} bar, relating to the dashed lines in Fig. 9). The inhomogeneity can be clearly seen by the lack of symmetry either side of $180°$ for both F and P. Fig. 11 gives the same output but for a clear atmosphere, which appears symmetric about $180°$. It can be seen that P peaks at $90°$ and $270°$, due to Rayleigh scattering by the atoms and molecules in the atmosphere. Fig. 12 gives the inhomogeneous model atmospheres with irregular rather than spherical particles at pressure layers of 0.01 bar and above.

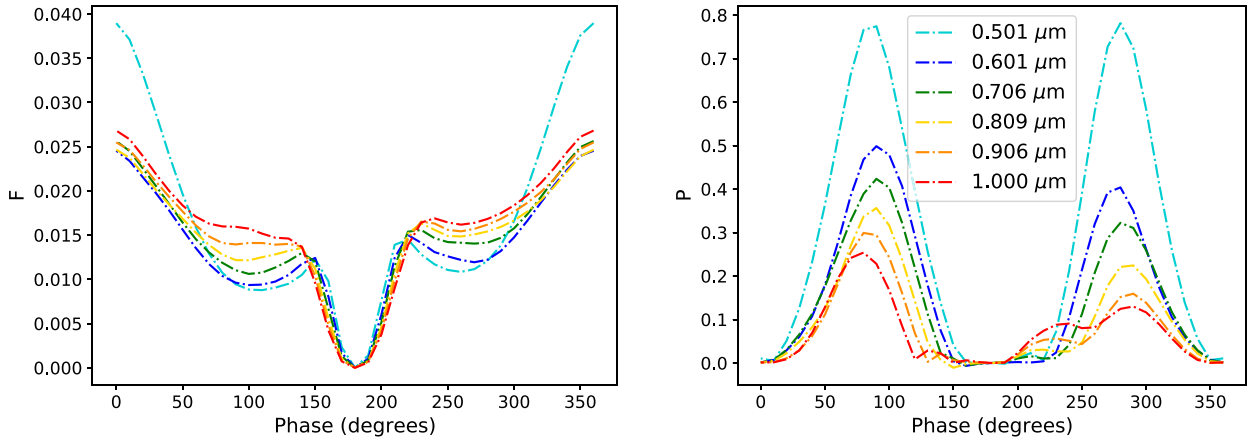---

[7]https://github.com/cdominik/optool
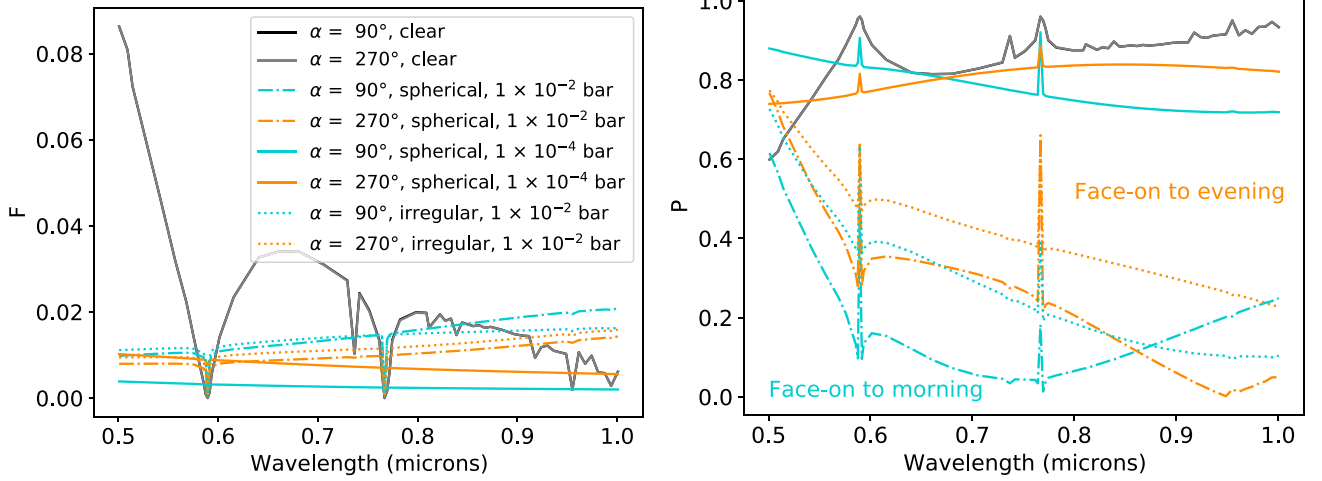
Figure 9. Reflected flux F (left) and degree of linear Polarization P (right) for our model inhomogeneous (i.e. varying as a function of longitude and latitude) WASP-96b atmosphere, assuming different properties for atmospheric regions $A - F$, split as illustrated by Fig. 2. The optical depth reaches unity due to clouds at the pressure level specified in the legend, that is, 1×10^{-2} bar (dash-dotted orange and turquoise lines) and 1×10^{-4} bar (solid orange and turquoise lines). A comparison to the same model setup (same pressure–temperature profiles and molecular compositions) but with completely clear atmospheres is shown. The clear atmospheres are nearly identical so cannot easily be distinguished here. The dotted lines are for model atmospheres which reach optical depth at 1×10^{-2} bar but with irregularly shaped particles ($f_{max} = 0.8$) from 0.01 bar and above. We consider orbital phases of α of 90 and 270°.

Figure 10. Reflected flux F (left) and degree of linear Polarization P (right) as a function of orbital phase α and at various wavelengths, for the inhomogeneous WASP-96b model atmosphere.
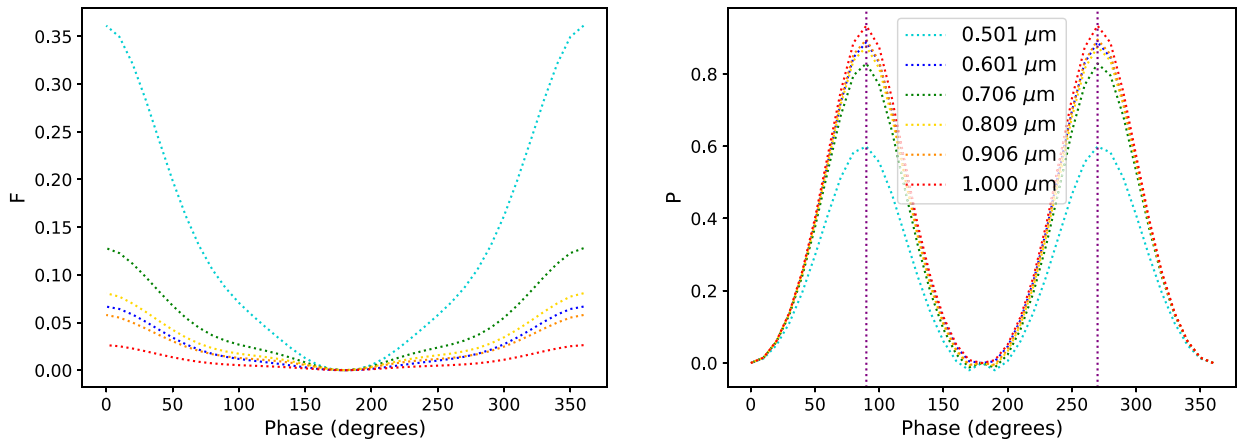
Figure 11. Reflected flux F (left) and degree of linear Polarization P (right) as a function of orbital phase α and at various wavelengths, for the inhomogeneous WASP-96b model atmosphere with a clear (no-cloud) atmosphere. Vertical lines at 90 and 270° are shown for reference.

Figure 12. Reflected flux F (left) and degree of linear Polarization P (right) as a function of orbital phase α and at various wavelengths, for the inhomogeneous WASP-96b model atmosphere with irregular instead of spherical particles for pressure layers of 0.01 bar and above.

6.3 Homogeneous model atmospheres: F and P as a function of wavelength for $\alpha = 90°$

In order to explore why the inhomogeneous atmosphere looks as it does for F and P, in Fig. 13 we show a series of models of homogeneous atmospheres (i.e. atmospheres which do not vary as a function of longitude and latitude, but only by altitude) of types A. . . F (where A. . . F are the six atmospheric regions as defined in Fig. 2). The models of Fig. 13 can be compared to the dashed lines in Fig. 9, which gives the equivalent inhomogeneous atmosphere. There, the $\alpha = 90°$ model has contributions from atmospheric regions D, E, A, and F (i.e. the morning side of the planet), while the $\alpha = 90°$ model has contributions from regions B, C, A, and F (the evening side). We note from Fig. 13 that atmospheric region B and E are very similar to one another, as are A and C. This is due to the hotspot shift away from the substellar point and towards the warmer evening terminator, which is a result of strong equatorial winds driven by the tidally locked nature of the planet.

In order to now focus on one atmospheric type at a time, we focus on region B (around the evening terminator) and D (around the morning terminator). Figs 14 and 15 show F and P for some homogeneous atmospheres, using the atmospheric setup for region B (Fig. 14) and D (Fig. 15). The model with mixed composition clouds are shown (labelled as all species), along with the same setup but with single materials only used to form the clouds. We note that we use the same particle size distribution for all single-species scenarios here in order to offer a more direct comparison to the mixed-material scenario, but the single-particle models are purely theoretical and not based on physically motivated model atmospheres. See subsection 4.3.1 for more discussion on particle size distributions. It can be seen from Figs 14 and 15 that the model WASP-96b atmosphere is largely dominated by the optical properties of the Fe-bearing species which are used to form the mixed-composition clouds. For Fig. 14 in particular, the atmosphere with mixed-composition clouds and FeO-only clouds are nearly identical in F, but differ in P. The flux as a function of wavelength for a homogeneous atmosphere of type B is almost identical to the same model atmosphere but with FeO used to form all cloud particles, instead of the mixed cloud particles (see subsection 4.2). The examples shown in Figs 14 and 15 are for clouds made purely of Al2O3, Fe2O3, FeO, Mg2SiO4, or MgO. Such atmospheres have a high-SSA across all wavelengths (see Fig. 16), so a significant fraction of the incoming stellar light would be reflected out, some of it towards the observer, before it can be absorbed. It can be seen from

Fig. 16 that the optical properties of Fe_2SiO_4 lead it to share more similarities with the silicate and oxide species than the iron species.

As for the inhomogeneous atmospheres, we also explore homogeneous atmospheres using irregularly shaped instead of spherical cloud particles. Fig. 17 shows F (left) and degree of linear Polarization P (right) for a model homogeneous planet based on WASP-96b at $\alpha = 90°$ assuming atmospheric type B only, but with varying irregularity of the cloud particles. The value of f_{max} indicates the irregularity of the particle, with 0 a sphere (red) and higher values being more irregular. The effect of using irregular instead of spherical particles can be clearly seen.

Figs 18 – 20 give an indication of how the particle size distribution affects F and P as a function of wavelength. All three figures give F and P as a function of wavelength at $\alpha = 90°$ for model homogeneous atmospheres of type B. Fig. 18 uses a Gaussian particle size distribution with average particle size 0.25 μm and standard deviation 2.5×10^{-4} for all models, while Fig. 19 uses a Gaussian particle size distribution with average particle size 0.1 μm and standard deviation 0.01 for all models. Both present 11 different models, each with a single species used to form the clouds, as labelled. Fig. 20 focuses on model atmospheres each with only Mg_2SiO_4 used to form the clouds, but this time with varying parameters used for the Gaussian size distributions.

6.4 Homogeneous model atmospheres: F and P as a function of orbital phase for selected wavelengths

Appendix Figs B4 and B5 give the phase curves (i.e. variation of F or P with orbital phase) of different homogeneous atmospheres for selected wavelengths. All panels are assuming atmosphere type B, with the majority of the panels showing atmospheres with clouds made up of a single species (Al_2O_3, Fe_2O_3, FeO, Mg_2SiO_4, MgO) only. These are the same models as in Fig. 14. Phase curves for a homogeneous planet with atmosphere type B but containing clouds made up of mixed species (as described in subsection 4.2.2) are shown for comparison. It can be seen that different materials give different signatures, particularly when looking at the degree of linear Polarization P. Note the different scales on the y-axis; those which are less reflective such as FeO and Fe_2O_3 are also generally more highly polarizing than the other more reflective materials.
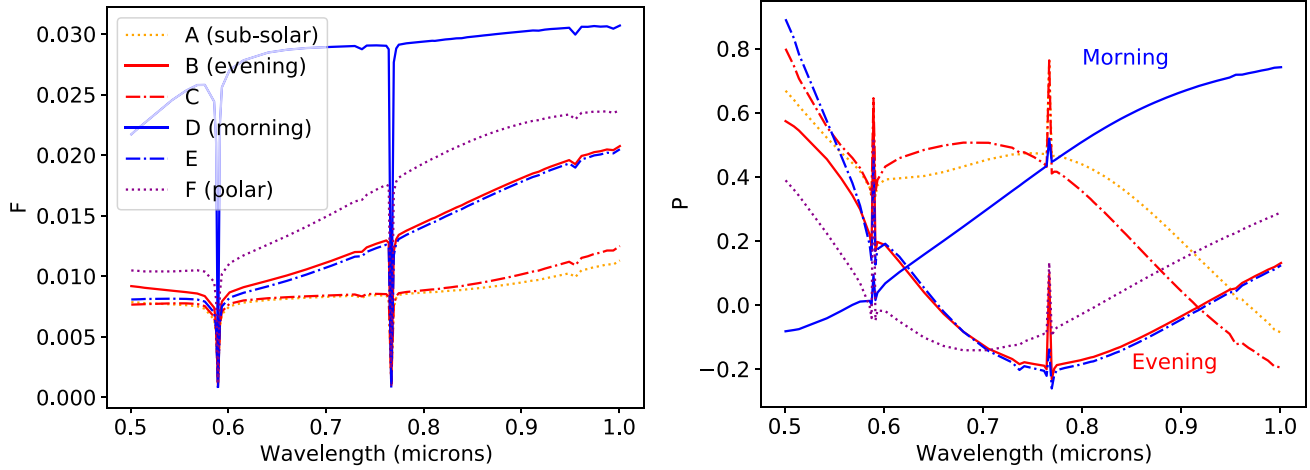
Figure 13. Reflected flux F (left) and degree of linear Polarization P (right) for 6 model homogeneous planets, each assuming a full atmosphere covered by one atmospheric region (A – F), as labelled. Region A covers the region around the substellar point, B the hotter evening terminator, and D the cooler morning terminator.
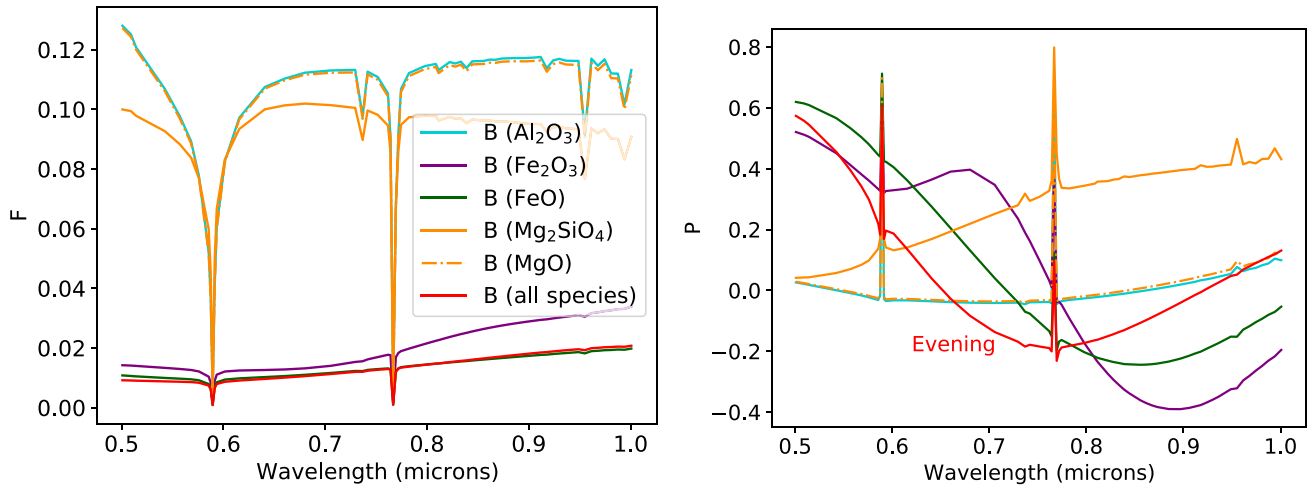
Figure 14. Reflected flux F (left) and degree of linear Polarization P (right) for model homogeneous planets based on WASP-96b at $\alpha = 90°$ assuming atmospheric type B (around the evening terminator) only. Some examples of clouds made of single materials only are shown. F and P for a homogeneous atmosphere with the full atmospheric setup for region B are shown for comparison (i.e. with clouds formed from mixed materials). In this case all size distributions of different layers for the single species cases are the same as in the mixed composition atmosphere.

6.5 Geometric albedo

As introduced in subsection 2.7, the geometric albedo A_G as a function of wavelength can be found by looking at the reflected flux at $\alpha = 0°$. A_G is plotted in Fig. 21 for the full inhomogeneous atmosphere setup, and for the homogeneous atmosphere setup of type B. The latter either includes mixed-species used to form clouds, or only a single species used to form the clouds (A_2O_3, Fe_2O_3, FeO, Mg_2SiO_4, MgO). The geometric albedo of a population of around 20 hot gaseous exoplanets have been measured by studies such as Angerhausen, DeLarme & Morse (2015) and Esteves, De Mooij & Jayawardhana (2015), with the finding that the majority have albedos typically less than 0.15 in the Kepler bandpass ($0.42 – 0.91 \, \mu m$). Two notable exceptions are HAT-P-7b with a measured geometric albedo of 0.23 (Heng & Demory 2013) and Kepler-7b with 0.25 (Heng, Morris & Kitzmann 2021). In our models, it can be seen that the highly absorbing Fe-bearing species FeO causes the geometric albedo to be very low for both the full inhomogeneous atmosphere and the homogeneous mixed species atmosphere of type B. If only

species with similar properties to silicates and oxides like Al_2O_3, Fe_2O_3, Mg_2SiO_4, and MgO were included in the atmosphere then the geometric albedo (which can be measured from observations) would be much higher. We note that it is known that there can be errors in calculated wavelength-dependent planetary phase functions and albedos due to treating light as a scalar and not as a vector, by neglecting Polarization (Stam & Hovenier 2005). An investigation on the impact of cloud materials on measured geometric albedo warrants further investigation.

7 DISCUSSION OF RESULTS

7.1 Impact of effective refractive index of materials used to form clouds

As previously mentioned, the imaginary part of the refractive index k of cloud particles relates to absorption, while the real part n relates to scattering. Materials considered in this study which have high
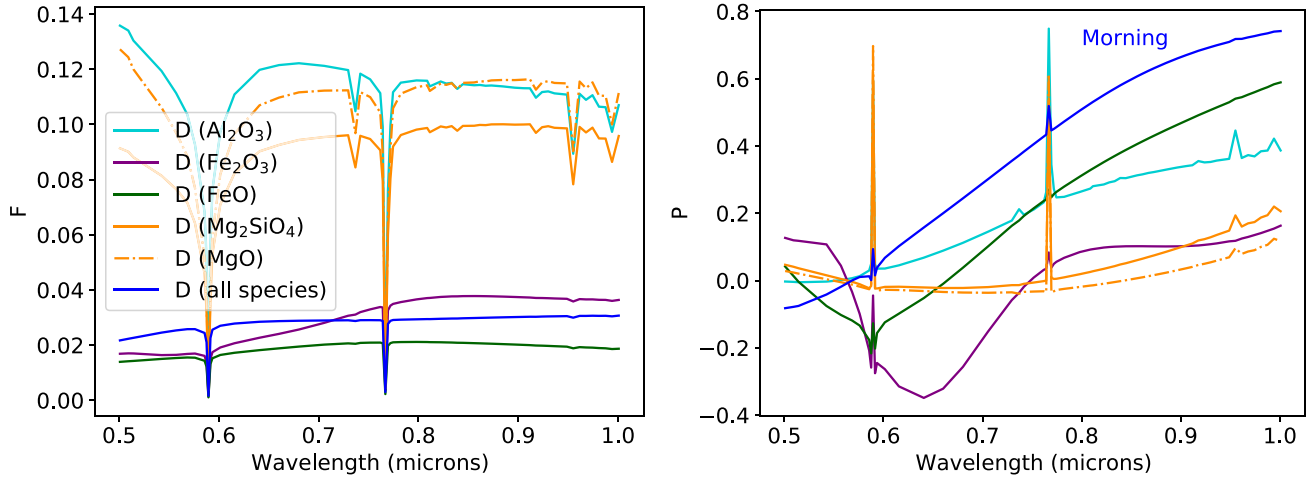
Figure 15. Reflected flux F (left) and degree of linear Polarization P (right) for model homogeneous planets based on WASP-96b at $\alpha = 90°$ assuming atmospheric type D (around the morning terminator) only. Some examples of clouds made of single materials only are shown. F and P for a homogeneous atmosphere with the full atmospheric setup for region D are shown for comparison (i.e. with clouds formed from mixed materials). In this case all size distributions of different layers for the single species cases are the same as in the mixed composition atmosphere.
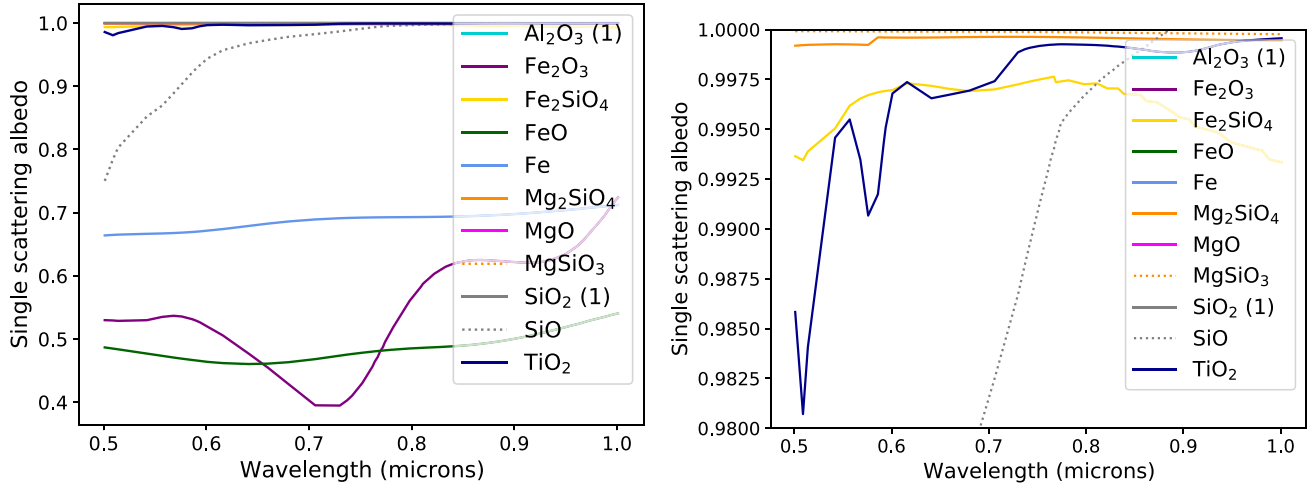
Figure 16. Single scattering albedo (ssa $= \frac{k_{scat}}{k_{ext}}$) of various species used in this study. The species with high values of the imaginary part of the refractive index k (Fe, Fe$_2$O$_3$, FeO) have lower values of SSA due to them being highly absorbing in comparison to the other species. Atmospheres with large mixing ratios of these iron-bearing have lower flux (due to high absorption) and relatively low degree of linear Polarization. The species in the legend with a (1) after their name are those with $k = 0$ and thus SSA $= 1$ for all wavelengths shown. The panel on the right is the same as the left but zoomed in for clarity.

values of k and relatively lower values of n (see Fig. 5) and thus low-SSAs (Fig. 16) are all Fe-bearing species (Fe, FeO, Fe$_2$O$_3$). Theoretical atmospheres composed of such species, as illustrated by Fig. 18, have relatively lower F across all wavelengths. Fig. 16 gives some insights into the scattering behaviour of particles formed from different materials as a function of wavelength. Fe$_2$O$_3$ for example has a SSA which varies significantly as a function of wavelength. The impact of Fe-bearing materials forming clouds in our model exoplanet atmospheres can be seen in Figs 14 and 15. The left panel of each shows F as a function of wavelength for single species compared to the full setups (including mixed cloud species) for homogeneous atmosphere setups of type B or D, respectively. It can be seen that the models which include either the mixed cloud species or FeO only have much lower F across all wavelengths than those which include only Al$_2$O$_3$ or Mg$_2$SiO$_4$. This highlights the effect that Fe-bearing materials can have on the reflected flux, and therefore observed albedo, of hot transiting gas giants. Fe and Fe$_2$O$_3$

behave in a similar way to FeO, but interestingly Fe$_2$SiO$_4$ behaves in a similar way to the silicates or oxides, due to it's lower imaginary part of the refractive index k.

It can be seen that the refractive indices of the morning and evening terminators in Appendix Fig. B1 (top and middle) are similar for some pressure layers, but differ around 1×10^{-3} bar in particular. The refractive indices at the substellar point are very similar to the evening terminator for all pressure layers shown. The imaginary component of the refractive index k is higher in the hotter evening region than the cooler morning region. From Fig. 6 it can be seen that this is likely due to the large proportion of clouds formed from Fe extending higher in to the atmosphere. Fig. 13 (left), demonstrates that for the hotter regions of the atmosphere which generally have a higher imaginary component of the refractive index k (from Appendix Fig. B1) also have lower F in comparison to the cooler regions. The imaginary component is slightly higher at lower wavelengths, which leads to a general trend of increasing flux with wavelength, as shown by
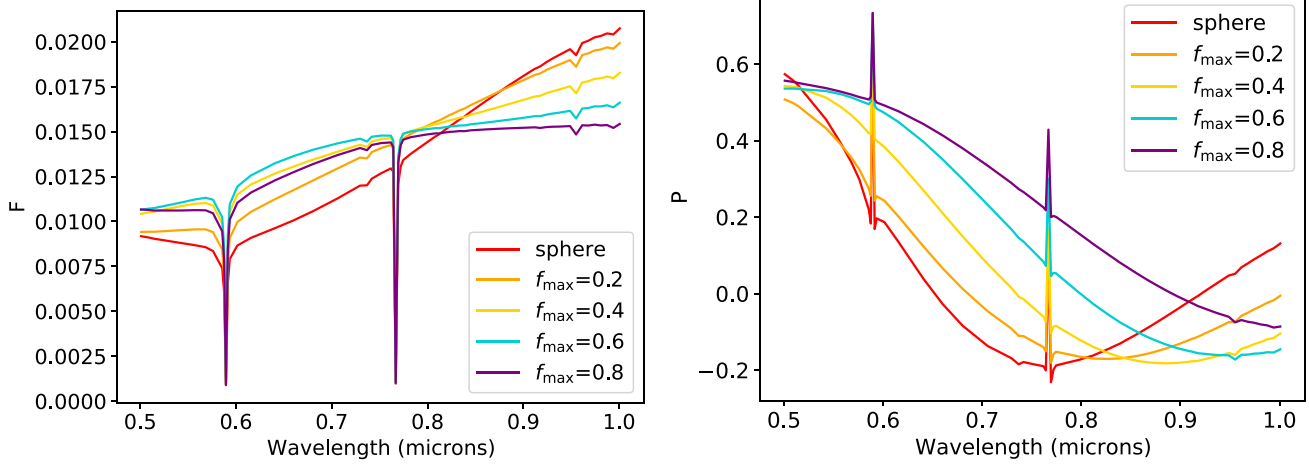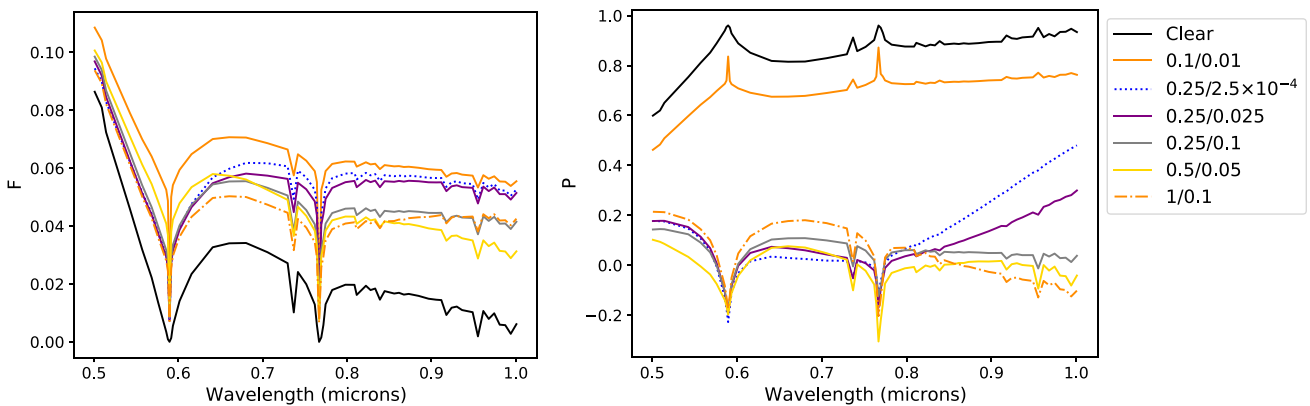
Figure 17. Reflected flux F (left) and degree of linear Polarization P (right) for a model homogeneous planet based on WASP-96b at $\alpha = 90°$ assuming atmospheric type B only, but with varying irregularity of the cloud particles. The value of f_{max} indicates the irregularity of the particle, with 0 a sphere (red) and higher values being more irregular.
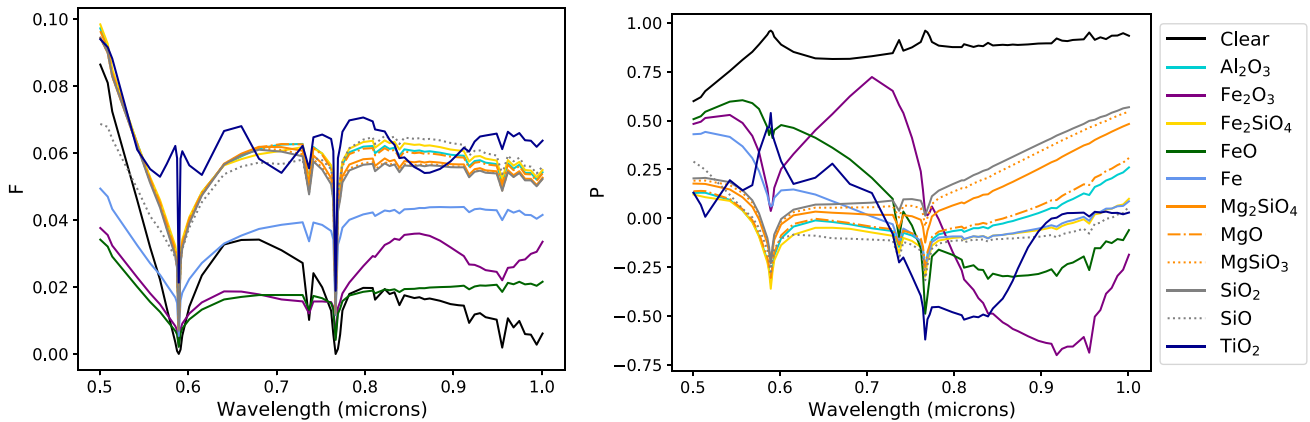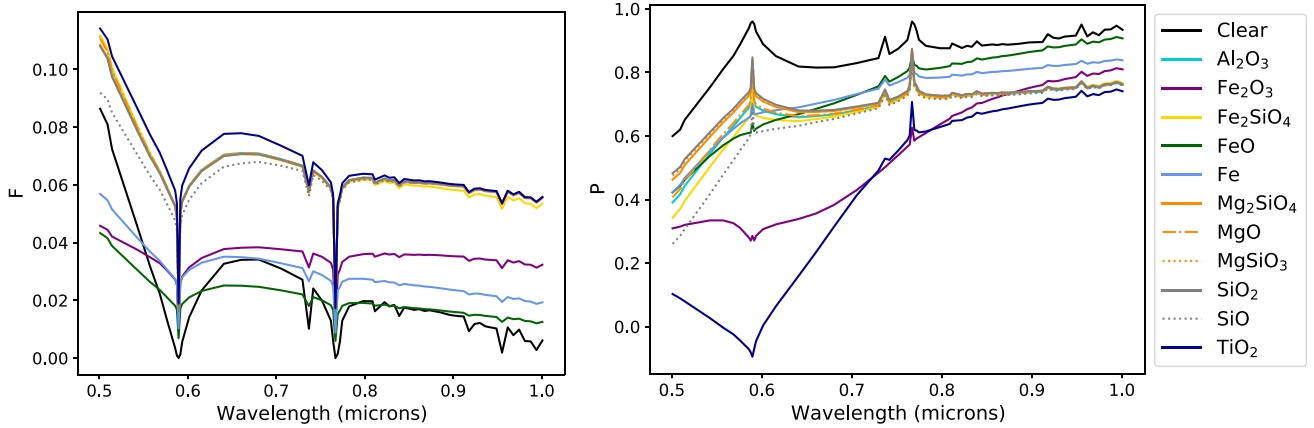
Figure 18. Reflected flux F (left) and degree of linear Polarization P (right) for a model homogeneous atmosphere based on WASP-96b at $\alpha = 90°$, using a different single material to form the clouds for each. A Gaussian size distribution is used, with $2.5 \times 10^{-4}\sigma$ standard deviation around an average particle size of $0.25\,\mu$m, for atmosphere type B.

Figure 20. Reflected flux F (left) and degree of linear Polarization P (right) for a model homogeneous atmosphere based on WASP-96b at $\alpha = 90°$, using a different single material Mg_2SiO_4 to form the clouds. Gaussian size distribution are used for each with the average particle size (in units of μm) and standard deviation σ as labelled.

Fig. 13 (left). The shape of F and P as a function of wavelength for homogeneous atmospheres composed of atmospheric region B, D, or A only (using the clouds formed from mixed materials for each region) can be seen from the single scattering properties of the materials used to form the clouds in these regions at various pressure layers, as shown in Appendix Fig. B6. Here, the single scattering

Figure 19. Reflected flux F (left) and degree of linear Polarization P (right) for a model homogeneous atmosphere based on WASP-96b at $\alpha = 90°$, using a different single material to form the clouds for each. A Gaussian size distribution is used, with 0.01σ standard deviation around an average particle size of $0.1\,\mu$m, for atmosphere type B.
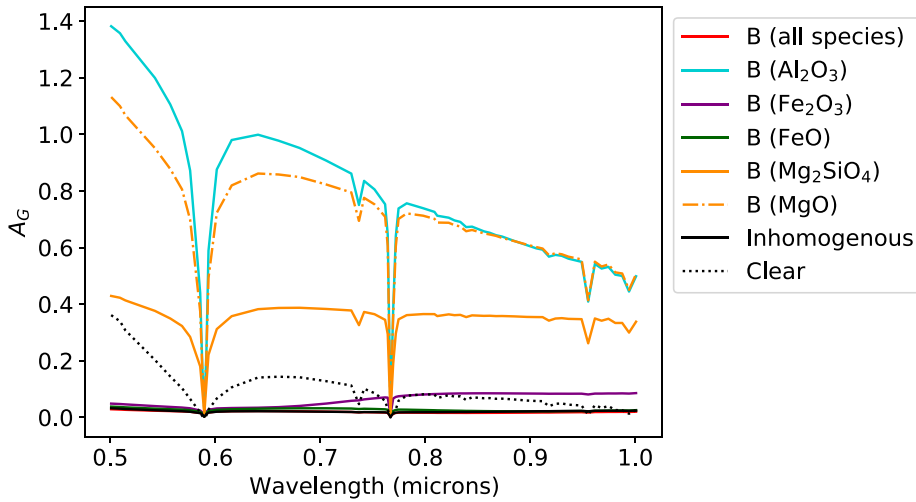
Figure 21. Geometric albedo A_G as a function of wavelength for: the full inhomogeneous setup including mixed-material clouds, the clear inhomogeneous setup, and model homogeneous planets assuming atmospheric type B (around the evening terminator) only. Homogeneous model atmosphere of atmospheric type B are also shown: either with all cloud species (i.e. with clouds formed from mixed materials), or with some examples of single materials only.

matrix elements F_{11} and $P = -\frac{F_{12}}{F_{11}}$ are plotted as a function of wavelength (see details in subsection 7.2).

7.2 Impact of clouds on the degree of linear Polarization

Different atmospheric layers are probed within (higher in the atmosphere) and outside (lower in the atmosphere) the atomic and molecular absorption features. If vertically inhomogeneous clouds are present in the atmosphere then different cloud layers are thus probed within and outside the absorption features. Gas particles scatter strongly at an angle of $90°$, as can be seen in Fig. 11. This scattering angle is largely relevant for orbital phases of $\alpha = 90°$ or $\alpha = 270°$. We therefore plot single scattering matrix elements F_{11} and $P = -\frac{F_{12}}{F_{11}}$ at $90°$ as a function of wavelength λ in order to gain some insight into why the models with mid-altitude cloud layers in Fig. 9 of P as a function of λ for $\alpha = 90°$ or $270°$ look like they do. This is demonstrated by Fig. 13, showing the contribution to P from different atmospheric regions A. . . F, and Appendix Fig. B6, showing the single scattering properties of the mixed-material cloud particles used to form each layer in regions B (evening), D

(morning), and A (substellar). Fig. B7 shows the single scattering properties of selected different materials, and so does not depend on the atmospheric setup of WASP-96b such as the temperature pressure profile. The only difference between atmosphere regions B (upper panels) and D (lower panels) in this case are the size distributions of the particles, which are based on the size distributions at 0.01 bar for these regions. Appendix Fig. B7 therefore really highlights the impact that size distribution alone can have on the scattering properties of a cloud material.

The atmosphere containing mixed-composition clouds in Fig. 14 has a low value of P between 0.7 and 0.8 μm. The behaviour around the absorption feature, where P dips just before and after the peak, is indicative of different atmospheric levels being probed here. Particles with different material composition and size distribution are in the atmosphere at different levels.

7.3 Particle size distributions

We use a Gaussian distribution to describe the sizes of the local particles in this work. Other particle size distributions are discussed

in various works such as Hansen & Travis (1974); de Rooij & van der Stap (1984); Samra (2022). Studies which use the cloud-model of Ackerman & Marley (2001) usually use a lognormal distribution (e.g. Lacy & Burrows 2020; Luna & Morley 2021), which was initially employed by Ackerman & Marley (2001) based on measurements of terrestrial cloud particles, while other works such as Powell et al. (2018, 2019) typically compute particle size distributions from first principles. A modified-gamma distribution, based on terrestrial water clouds (Deirmendjian 1964), is also sometimes used in atmospheric models (e.g. Pinhas & Madhusudhan 2017). Although particle distributions based on measured Earth cloud particles can be considered a reasonable assumption, it is tricky to know the exact nature of size distributions in exoplanetary atmospheres such as the one we are modelling here. One benefit of using a Gaussian size distribution is the ease of determining a broad versus narrow distribution, as well as computational requirements. For example, some distributions have very long tails and a few very large particles can lead to very lengthy radiative transfer computations while having only a small influence on the reflected light spectra (Hansen & Travis 1974), although we note some mentioned here such as the lognormal distribution can be considered relatively efficient. The impact of the particle size distribution on the reflected flux and Polarization warrants further exploration.

7.4 Close-in planets

Our focus is on characterizing close-in transiting exoplanets. Although we do not explicitly take it into account here, we are aware of expected deviations of F and P for extreme orbital phases α. This has been explored before by, for example, Palmer, Rossi & Stam (2017). They show the variation of F and P as a function of distance from the host star for hot Jupiter exoplanets around solar-type stars. Situations where the angular size of the host star in an exoplanet's sky is non-negligible are also investigated in Palmer (2019). They define close-in planets which start to be affected, largely at the extreme orbital phase angles, as those closer than 0.05 au, although the exact distance depends on the planet and star sizes also. With a semimajor axis of 0.045 au (Hellier et al. 2014), WASP-96b is very close to this cutoff and thus has potential to be affected by the geometry, although noticeably less than even closer-in planets at 0.005 or 0.01 au, as demonstrated by Palmer, Rossi & Stam (2017). Palmer (2019) find the flux to be particularly affected at extremes of orbital phase angle. Kostogryz et al. (2017) investigate the difference in flux and Polarization curves for transiting exoplanets in the cases of either plane parallel or a spherical stellar atmosphere used in models. They find that for most cases of known transiting systems the plane-parallel approximation can be safely used due to only a very small difference between the results using the two approaches. We therefore do not expect our resulting spectra as a function of wavelength which we typically take at orbital phases of $\alpha = 90°$ or $270°$ to be significantly affected by such affects, but for our results which show the variation of F or P with orbital phase at set values of wavelength, some caution should be exercised at the extreme values of phase (close to $0°$ and $180°$). This also applies to our figures of geometric albedo as a function of wavelength, although we do expect the difference to be small and for the general trends to hold. In all our models the geometry causes F to go to $0°$ at $180°$, but in reality there could be expected to be some scattered flux at such a phase angle for very close-in exoplanets.

There are other aspects of an exoplanet's orbit which we do not consider in the present study. For example, there is an expectation

that close-in exoplanets are more impacted by tidal deformation than those further out, and the rotation rate of these planets affect their oblateness. Palmer (2019) also investigate such effects and show, for example, that increasing the oblateness of a planet increases the amount of scattering at high atmospheric altitudes, which is typically expected to lead to an increase in the maximum degree of Polarization. We assume the orbital inclination angles of our model planets are $90°$. For reference, the inclination of WASP-96b has been measured very close to $90°$, at $85.6°$ (Hellier et al. 2014).

7.5 Temperature dependence of optical properties

Some studies have been done regarding the temperature dependence of the optical properties of various species, such as olivine, enstatite (Zeidler, Mutschke & Posch 2015), and corundum, spinel, and alpha-quartz (Zeidler, Posch & Mutschke 2013), although these studies are generally focused on larger wavelengths than in our study. Yang & Zhan (2020) found that the optical properties of forsterite (Mg_2SiO_4) undergo a blue shift with increasing pressure. More studies exploring the temperature dependence of materials used to form clouds would be beneficial to future work.

7.6 Porosity of cloud particles

As predicted by Samra et al. (2023), the atmosphere of WASP-96b will also be impacted by the porosity of the material used to form the cloud particles. We have not investigated this here, but it will be of interest to look into how different degrees of porosity of the cloud particles will affect F and P of a model WASP-96b planet.

8 CONCLUSION

WASP-96b is a relatively homogeneous planet, in terms of temperature contrast and differences in composition between morning and evening terminators, when compared to some other hotter gas giant planets which have been modelled using GCMs coupled with kinetic cloud modelling (Helling et al. 2021; Samra et al. 2023). The planet is expected to be relatively warm throughout, and thus expected to have clouds throughout the majority of the atmosphere. The molecular composition is relatively consistent across the morning and evening sides of the planet, with the exception of CH_4. We find that the degree of Polarization of reflected flux in particular is highly dependent on the types of clouds and the properties of the materials used to form them and therefore highlights even subtle differences between the morning and evening sides of the planet (i.e. when the planet is at $90°$ or $270°$ phase angle). We have investigated the effect of using irregularly shaped particles as opposed to assuming perfectly spherical particles in our models, and find there is a considerable difference in the modelled Polarization signals, in particular for an orbital phase of $90°$ (face-on to the cooler morning terminator). This highlights the importance of using more physically realistic models of cloud particles, in situations where the particles are expected to be more fluffy or irregular shaped. The exact shape of aerosol particles in such exotic atmospheres is not necessarily known at present, but it is an avenue which warrants future exploration. In either case, knowing the scattering properties of different shapes of particles will be an advantage when fitting models to observed spectra in the future.

In general we demonstrate in this study using the PolHEx code that we expect measuring the Polarization state of reflected flux of hot close-in transiting planets to give detailed insights into the atmosphere. It is an extremely complementary tool to analysing

transmission and emission spectroscopy observations of the same exoplanets, as it is sensitive to different components of an exoplanet atmosphere, most notably the material composition of clouds and their size distribution.

ACKNOWLEDGEMENTS

DATA AVAILABILITY

The data underlying this article will be shared on reasonable request to the corresponding author.

REFERENCES

Ackerman A. S., Marley M. S., 2001, ApJ, 556, L872
Ahrer E.-M. et al., 2023, Nature, 614, 653
Alderson L. et al., 2023, Nature, 614, 664
Allard N. F., Spiegelman F., Kielkopf J. F., 2016, A&A, 589, 21
Allard N. F., Spiegelman F., Leininger T., Mollière P., 2019, A&A, 628, 120
Angerhausen D., DeLarme E., Morse J. A., 2015, PASP, 127, 1113
Azzam A. A. A., Yurchenko S. N., Tennyson J., Naumenko O. V., 2016, MNRAS, 460, 4063
Baeyens R., Decin L., Carone L., Venot O., Agúndez M., Mollière P., 2021, MNRAS, 505, 5603
Bailey J., Cotton D. V., Kedziora-Chudczer L., De Horta A., Maybour D., 2020, Publ. Astron. Soc. Aust., 37, e004
Bailey J. et al., 2021, MNRAS, 502, 2331
Bailey J., Kedziora-Chudczer L., Bott K., 2018, MNRAS, 480, 1613
Bailey J., Kedziora-Chudczer L., Cotton D. V., Bott K., Hough J. H., Lucas P. W., 2015, MNRAS, 449, 3064
Barstow J. K., Aigrain S., Irwin P. G. J., Hackler T., Fletcher L. N., Lee J. M., Gibson N. P., 2014, ApJ, 786, L154
Batalha N. E., Marley M. S., Lewis N. K., Fortney J. J., 2019, ApJ, 878, L70
Berdyugina S. V., Berdyugin A. V., Fluri D. M., Piirola V., 2007, ApJ, 673, L83
Berdyugina S. V., Berdyugin A. V., Fluri D. M., Piirola V., 2011, ApJ, 728, L6
Berdyugina S. V., Kuhn J. R., Harrington D. M., vSantl Temkiv T., Messersmith E. J., 2016, International Journal of Astrobiology, 15, 45
Bott K., Bailey J., Cotton D. V., Kedziora-Chudczer L., Marshall J. P., Meadows V. S., 2018, AJ, 156, 293
Bott K., Bailey J., Kedziora-Chudczer L., Cotton D. V., Lucas P. W., Marshall J. P., Hough J. H., 2016, MNRASL, 459, L109
Bouret J.-C. et al., 2018, Space Telescopes and Instrumentation 2018: Ultraviolet to Gamma Ray, 10699, 851
Bouwman J. et al., 2023, PASP, 135, 038002
Bruggeman D. A. G., 1935, Annalen der Physik, 416, 636
Carone L. et al., 2020, MNRAS, 496, 3582
Chandrasekhar S., 1950, Quarterly Journal of the Royal Meteorological Society, 76, 498
Chubb K. L. et al., 2021, A&A, 646, 21
Chubb K. L., Min M., 2022, A&A, 665, 2
Cotton D. V., Marshall J. P., Bailey J., Kedziora-Chudczer L., Bott K., Marsden S. C., Carter B. D., 2017, MNRAS, 467, 873
de Boer J. et al., 2020, A&A, 633, 63
de Haan J. F., Bosma P., Hovenier J., 1987, A&A, 183, 371
de Kok R. J., Helling C., Stam D. M., Woitke P., Witte S., 2011, A&A, 531, 67
de Rooij W. A., van der Stap C. C. A. H., 1984, A&A, 131, 237
Deirmendjian D., 1964, Appl. Opt., 3, 187

Dominik C., Min M., Tazaki R., 2021, OpTool: Command-line driven tool for creating complex dust opacities, Astrophysics Source Code Library, record ascl:2104.010
Donati J. F., Catala C., Landstreet J. D., Petit P., 2006, in Casini R., Lites B. W.eds, Astronomical Society of the Pacific Conference SeriesVol. 358, Solar Polarization 4. p. 362
Dorn R. J. et al., 2023, A&A, 671, 24
Dorschner J., Begemann B., Henning T., Jaeger C., Mutschke H., 1995, A&A, 300, 503
Esteves L. J., De Mooij E. J., Jayawardhana R., 2015, ApJ, 804, L150
Fauchez T., Rossi L., Stam D. M., 2017, ApJ, 842, L41
Feinstein A. D. et al., 2023, Nature, 614, 670
Fossati L. et al., 2019, Bulletin of the American Astronomical Society, 51, 33
Gasman D., Min M., Chubb K. L., 2022, A&A, 659, 114
Gisler D. et al., 2004, Ground-based Instrumentation for Astronomy, 5492, 463
Grainger D. et al., 2023, in DonGrainger, DanPeters, LievenClarisse, HervéHerbin, eds. Aerosol Refractive Index Archive (ARIA) database, ARIA database
Groff T. D. et al., 2021, Space Telescopes and Instrumentation 2020: Optical, Infrared, and Millimeter Wave, 11443, 114433D
Groot A., Rossi L., Trees V. J. H., Cheung J. C. Y., Stam D. M., 2020, A&A, 640, 121
Hansen J. E., Hovenier J. W., 1974, Journal of Atmospheric Sciences, 31, 1137
Hansen J. E., Travis L. D., 1974, Space science reviews, 16, 527
Hellier C. et al., 2014, MNRAS, 440, 1982
Helling C., 2022, preprint (arXiv:2205.00454)
Helling C. et al., 2021, A&A, 649, 44
Helling C. et al., 2023, A&A, 671, 122
Helling C., Gourbin P., Woitke P., Parmentier V., 2019, A&A, 626, 133
Heng K., Demory B.-O., 2013, ApJ, 777, L100
Heng K., Morris B. M., Kitzmann D., 2021, Nature Astron., 5, 1001
Henning T., Begemann B., Mutschke H., Dorschner J., 1995, A&AS, 112, 143
Hovenier J. W., 1970, A&A, 7, 86
Hovenier J. W., van der Mee C. V. M., 1983, A&A, 128, 1
Hovenier J. W., Van Der Mee C., Domke H., 2004, Transfer of polarized light in planetary atmospheres: basic concepts and practical methods, Astrophysics and Space Science Library (ASSL), Vol. 318, Springer, Netherlands
Jäger C., Dorschner J., Mutschke H., Posch T., Henning T., 2003, A&A, 408, 193
Joos F., Schmid H. M., 2007, A&A, 463, 1201
Karalidi T., Stam D. M., 2012, A&A, 546, 56
Karalidi T., Stam D. M., Guirado D., 2013, A&A, 555, 127
Karalidi T., Stam D. M., Hovenier J. W., 2012, A&A, 548, 90
Kawashima Y., Rugheimer S., 2019, AJ, 157, 213
Kemp J. C., Henson G. D., Steiner C. T., Powell E. R., 1987, Nature, 326, 270
Kitzmann D., Heng K., 2017, MNRAS, 475, 94
Kołos W., Wolniewicz L., 2004, The Journal of Chemical Physics, 46, 1426
Kostogryz N. M., Yakobchuk T. M., Berdyugina S. V., Milic I., 2017, A&A, 601, 6
Kramida A., Ralchenko Y., Reader J., 2013, NIST Atomic Spectra Database—Version 5
Krenn A. F. et al., 2023, A&A, 672, 24
Kuščer I., Ribarič M., 1959, Optica Acta: International Journal of Optics, 6, 42
Lacy B. I., Burrows A., 2020, ApJ, 904, L25
Li G., Gordon I. E., Rothman L. S., Tan Y., Hu S.-M., Kassi S., Campargue A., Medvedev E. S., 2015, ApJS, 216, 15
Lothringer J. D. et al., 2022, Nature, 604, 49
Luna J. L., Morley C. V., 2021, ApJ, 920, L146
MacDonald R. J., Marley M. S., Fortney J. J., Lewis N. K., 2018, ApJ, 858, L69
McLean W. et al., 2017, A&A, 601, 142

Meinke K., Stam D. M., Visser P. M., 2022, A&A, 664, 59

Mie G., 1908, Annalen der Physik, 330, 377

Millar-Blanchaer M. A. et al., 2020, ApJ, 894, L42

Millar-Blanchaer M. et al., 2018, White paper submitted to the Committee on Exoplanet Science Strategy, National Academies of Sciences, Engineering, and Medicine, Washington, D.C.

Min M., Hovenier J. W., de Koter A., 2003, A&A, 404, 35

Min M., Hovenier J. W., de Koter A., 2005, A&A, 432, 909

Mishchenko M. I., Dlugach J. M., Liu L., 2016, J. Quant. Spectrosc. Radiat. Transfer, 178, 284

Mishchenko M. I., Travis L. D., Lacis A. A., 2002, Scattering, Absorption, and Emission of Light by Small Particles. Cambridge Univ. Press, Cambridge

Mishchenko M. I., Zakharova N. T., Khlebtsov N. G., Videen G., Wriedt T., 2017, J. Quant. Spectrosc. Radiat. Transfer, 202, 240

Mollière P., van Boekel R., Bouwman J., Henning T., Lagage P.-O., Min M., 2017, A&A, 600, 10

Muñoz A. G., 2018, ApJ, 854, L108

Mutschke H. et al., 2023, Database of Optical Constants for Cosmic Dust, compilation and website by Harald Mutschke and Jürgen Weiprecht. OC DB

Nikolov N. K. et al., 2022, MNRAS, 515, 3037

Nikolov N. et al., 2018, Nature, 557, 526

Ormel C. W., Min M., 2019, A&A, 622, 121

Palik E. D., 2012, Handbook of Optical Constants of Solids: Vol 2. Academic Press, New York

Palmer C., 2019, Delft University of Technology Master Thesis

Palmer C., Rossi L., Stam D., 2017, in EPSC Abstracts, 11, EPSC2017–613, European Planetary Science Congress 2017Geometric effects on the flux and polarization signals of Jupiter-sized exoplanets

Penndorf R., 1957, J. Opt. Soc. Am., 47, 176

Pinhas A., Madhusudhan N., 2017, MNRAS, 471, 4355

Piskunov N. et al., 2011, The Messenger, 143

Polyansky O. L., Kyuberis A. A., Zobov N. F., Tennyson J., Yurchenko S. N., Lodi L., 2018, MNRAS, 480, 2597

Powell D., Louden T., Kreidberg L., Zhang X., Gao P., Parmentier V., 2019, 170 ApJ, L887

Powell D., Zhang X., Gao P., Parmentier V., 2018, ApJ, 860, L18

Radica M. et al., 2023, MNRAS, 524, 835

Rayleigh O. M., 1918, The London, Edinburgh, and Dublin Philosophical Magazine and Journal of Science, 35, 373

Rossi L., Berzosa-Molina J., Stam D. M., 2018, A&A, 616, 147

Rossi L., Marcq E., Montmessin F., Fedorova A., Stam D., Bertaux J.-L., Korablev O., 2015, Planet. Space Sci., 113–114, 159

Rossi L., Stam D. M., 2017, A&A, 607, 57

Rossi L., Stam D. M., 2018, A&A, 616, 117

Rustamkulov Z. et al., 2023, Nature, 614, 659

Samra D., 2022, University of St Andrews PhD Thesis

Samra D., Helling C., Birnstiel T., 2022, A&A, 663, 47

Samra D., Helling C., Chubb K. L., Min M., Carone L., Schneider A. D., 2023, A&A, 669, 142

Samra D., Helling C., Min M., 2020, A&A, 639, 107

Schmude Richard J., 2008, Journal of the Association of Lunar and Planetary Observers, the Strolling Astronomer, 51, 25

Schneider A. D., Carone L., Decin L., Jørgensen U. G., Mollière P., Baeyens R., Kiefer S., Helling C., 2022, A&A, 664, 56

Seager S., Whitney B. A., Sasselov D. D., 2000, ApJ, 540, L504

Sparks W. B., Parenteau M. N., Blankenship R. E., Germer T. A., Patty C. H. L., Bott K. M., Telesco C. M., Meadows V. S., 2021, Astrobiology, 21, 219

Stam D. M., 2008, A&A, 482, 989

Stam D. M., De Rooij W. A., Cornet G., Hovenier J. W., 2006, A&A, 452, 669

Stam D. M., Haan J. F. D., Hovenier J. W., Stammes P., 1999a, J. Geophys. Res., 104, 16843

Stam D. M., De Haan J. F., Hovenier J. W., Stammes P., 1999b, J. Geophys. Res., 104, 16843

Stam D. M., Hovenier J. W., 2005, A&A, 444, 275

Stam D. M., Hovenier J. W., Waters L. B. F. M., 2004, A&A, 428, 663

Stam D., De Haan J., Hovenier J., Stammes P., 2000, J. Quant. Spectrosc. Radiat. Transfer, 64, 131

Strassmeier K. et al., 2015, Astron. Nachr., 336, 324

Takahashi J., Matsuo T., Itoh Y., 2017, A&A, 599, 56

Taylor J. et al., 2023, MNRAS, 524, 817

Tazaki R., Tanaka H., 2018, ApJ, 860, L79

Tinyanont S. et al., 2019, Polarization Science and Remote Sensing IX, 11132, 48

Tomasko M., Doose L., 1984, Icarus, 58, 1

Trees V. J. H., Stam D. M., 2019a, A&A, 626, 129

Trees V. J. H., Stam D. M., 2019b, A&A, 626, 129

Trees V. J. H., Stam D. M., 2022, A&A, 664, 172

Triaud A., 2005, Private Communication

Vaughan S. R. et al., 2023, MNRAS, 524, 5477

Wakeford H. R., Sing D. K., 2015, A&A, 573, 122

West R. A., Dumont P., Hu R., Natraj V., Breckinridge J., Chen P., 2022, ApJ, 940, 183

West R. A., Smith P. H., 1991, Icarus, 90, 330

Wolfram, 2022, Mathematica, Version 13.2, https://www.wolfram.com/mathematica

Wong I. et al., 2021, AJ, 162, 127

Yang X., Zhan Q., 2020, Molecular Simulation, 46, 805

Yurchenko S. N., Amundsen D. S., Tennyson J., Waldmann I. P., 2017, A&A, 605, 95

Yurchenko, Sergei N., Al-Refaie, Ahmed F., Tennyson, Jonathan, 2018, A&A, 614, 131

Yurkin M. A., Hoekstra A. G., 2011, J. Quant. Spectrosc. Radiat. Transfer, 112, 2234

Zeidler S., Mutschke H., Posch T., 2015, ApJ, 798, L125

Zeidler S., Posch T., Mutschke H., 2013, A&A, 553

Zeidler S., Posch T., Mutschke H., Richter H., Wehrhan O., 2011, A&A, 526, 68

# APPENDIX A: DETECTABILITY CALCULATIONS

Here, we demonstrate the detectability of the models presented in this paper for hot gaseous exoplanet WASP-96b. For this we first use equation (11) to compute the total reflected Flux arriving at the observer on (or near) Earth $F_p(\lambda, \alpha)$. We use cgs units for all parameters. To compute the stellar surface flux, we assume that the luminosity of a G8 star such as WASP-96 (Hellier et al. 2014) is $0.68\,L_\odot$, which translates to a surface flux of $3.88 \times 10^{10}\,\mathrm{erg\,s^{-1}\,cm^2}$. This corresponds to a maximum reflected planetary flux arriving to the observer F_p of $6.57 \times 10^{-15}\,\mathrm{erg\,s^{-1}\,cm^2}$. We can scale this against the total stellar flux arriving at the observer F_s using the relation

$$F_s = \frac{L}{4\pi d^2}, \qquad (A1)$$

where L is the stellar luminosity (erg s^{-1}), and d is the stellar-Earth distance (cm). This gives $F_s = 1.72 \times 10^{-10}\,\mathrm{erg\,s^{-1}\,cm^2}$. If we scale the maximum value of F_p with this we get $\frac{F_p}{F_s} = 38$ ppm. Using typical values of F and P from this figures shown in this paper gives us an approximate range of typical values for $\frac{P}{F_s}$ of $0.1 - 30$ ppm. This is called the 'observed Polarization' in Bailey et al. (2015) (i.e. Polarization as a fraction of light from the star). The HIPPI-2 instrument can measure a polarized signal with a precision of around 3.5 ppm (Bailey et al. 2020), with higher precisions expected from potential future instruments.

APPENDIX B: ADDITIONAL FIGURES
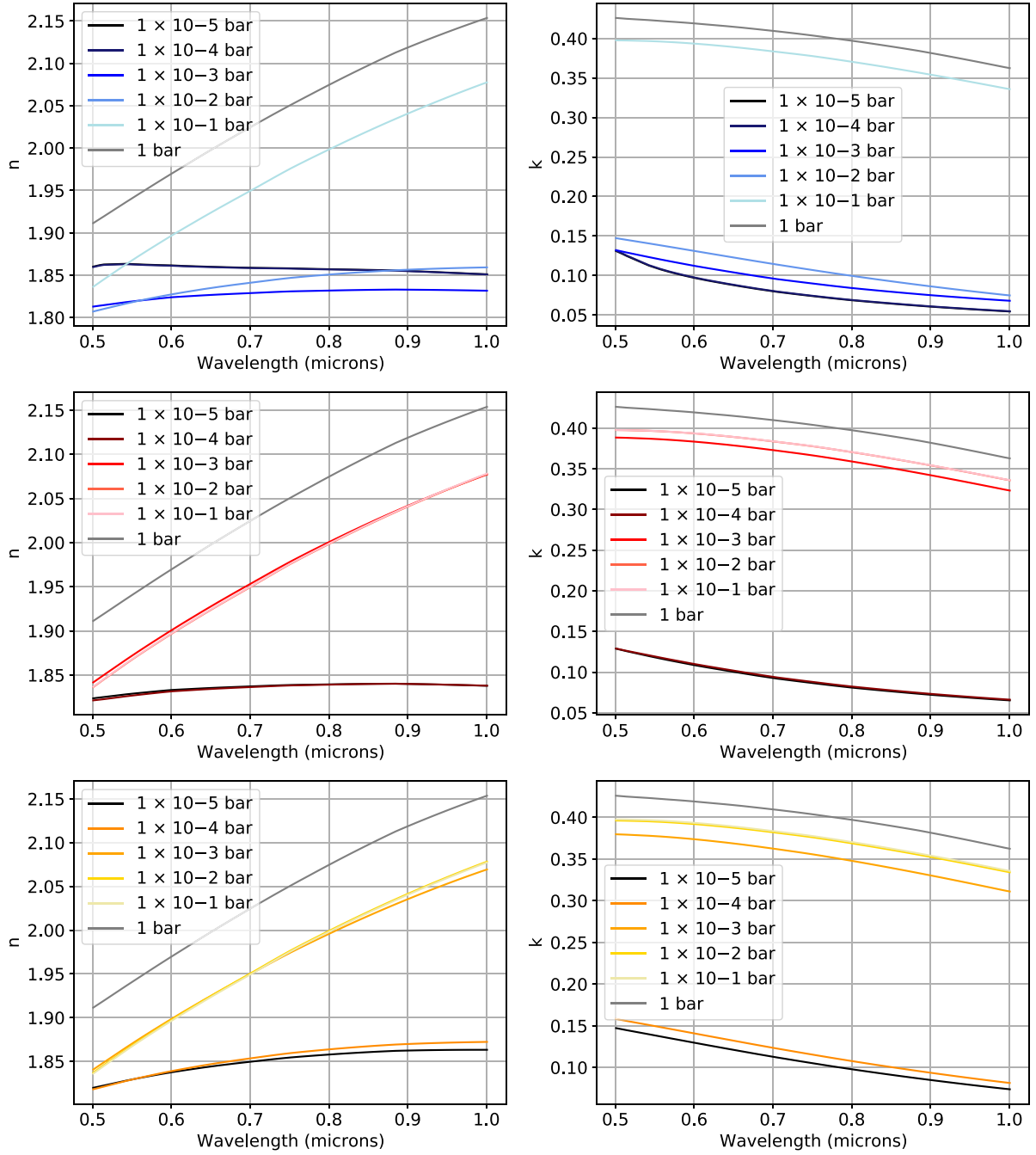
Figure B1. Complex refractive indices (real n and imaginary k component) of combined materials to form clouds as a function of wavelength for different atmospheric regions and pressure layers. Top: region D, $-90°/0°$ (morning). Middle: region B, $90°/0°$ (evening), Bottom: region A: $0°/0°$ (substellar point).
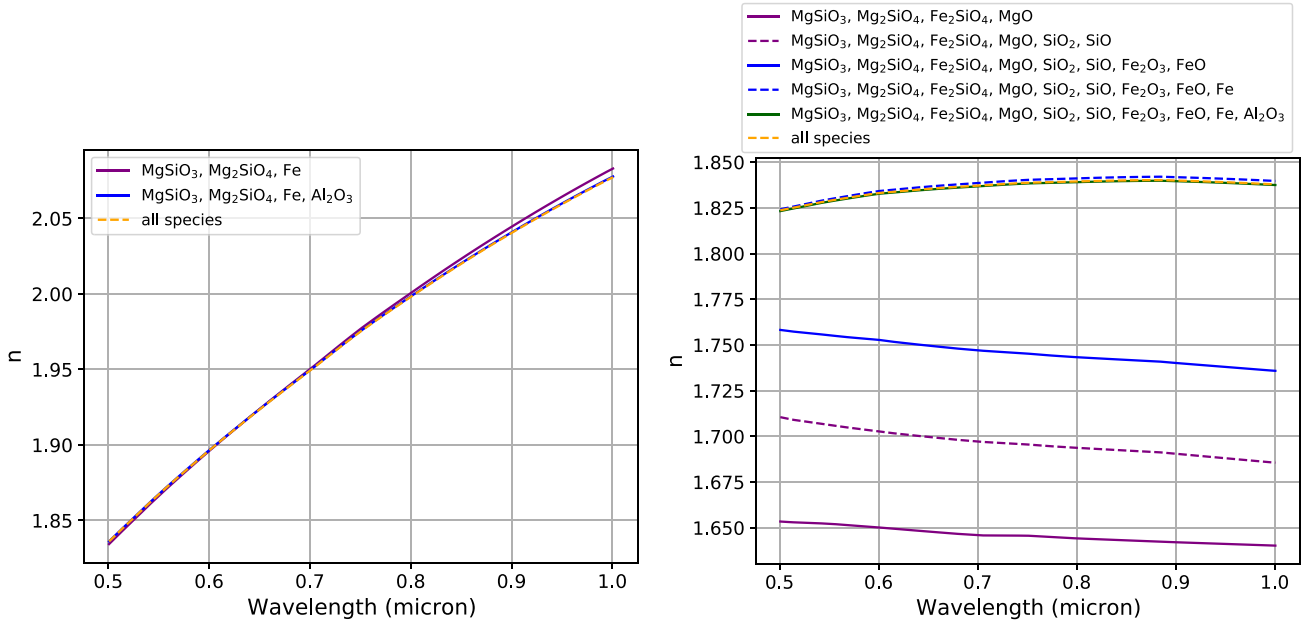
Figure B2. The real *n* components of the complex refractive indices of various amounts of combined materials to form clouds as a function of wavelength for region B 90°/0° (evening) and pressure layers 1×10^{-1} bar (left) and 1×10^{-4} bar (right).
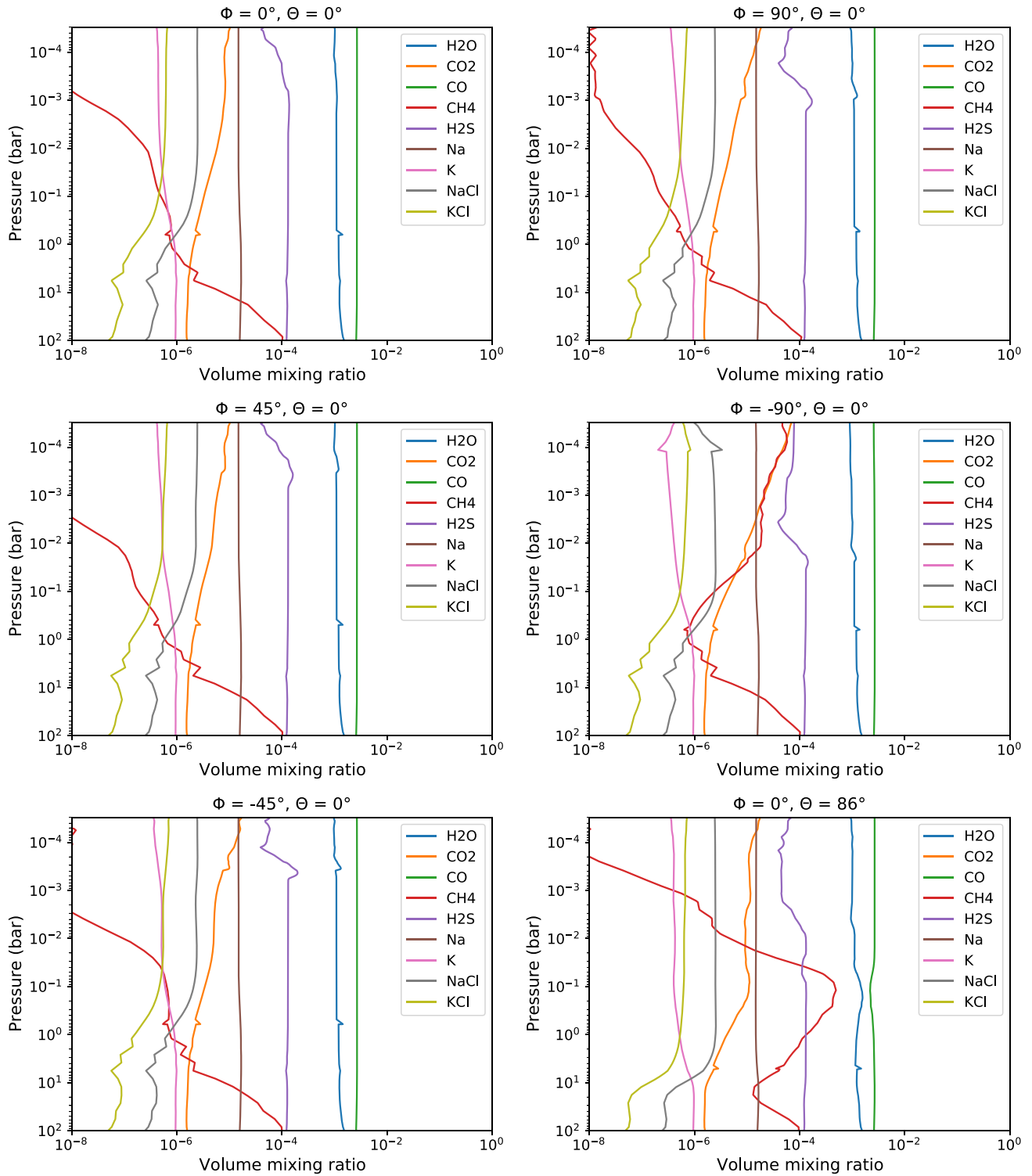
Figure B3. Molecular and atomic concentrations $\frac{n_i}{n_{tot}}$ for models of WASP-96b used in this work as a function of pressure, and at various longitude and latitude points, as labelled in each sub-plot.
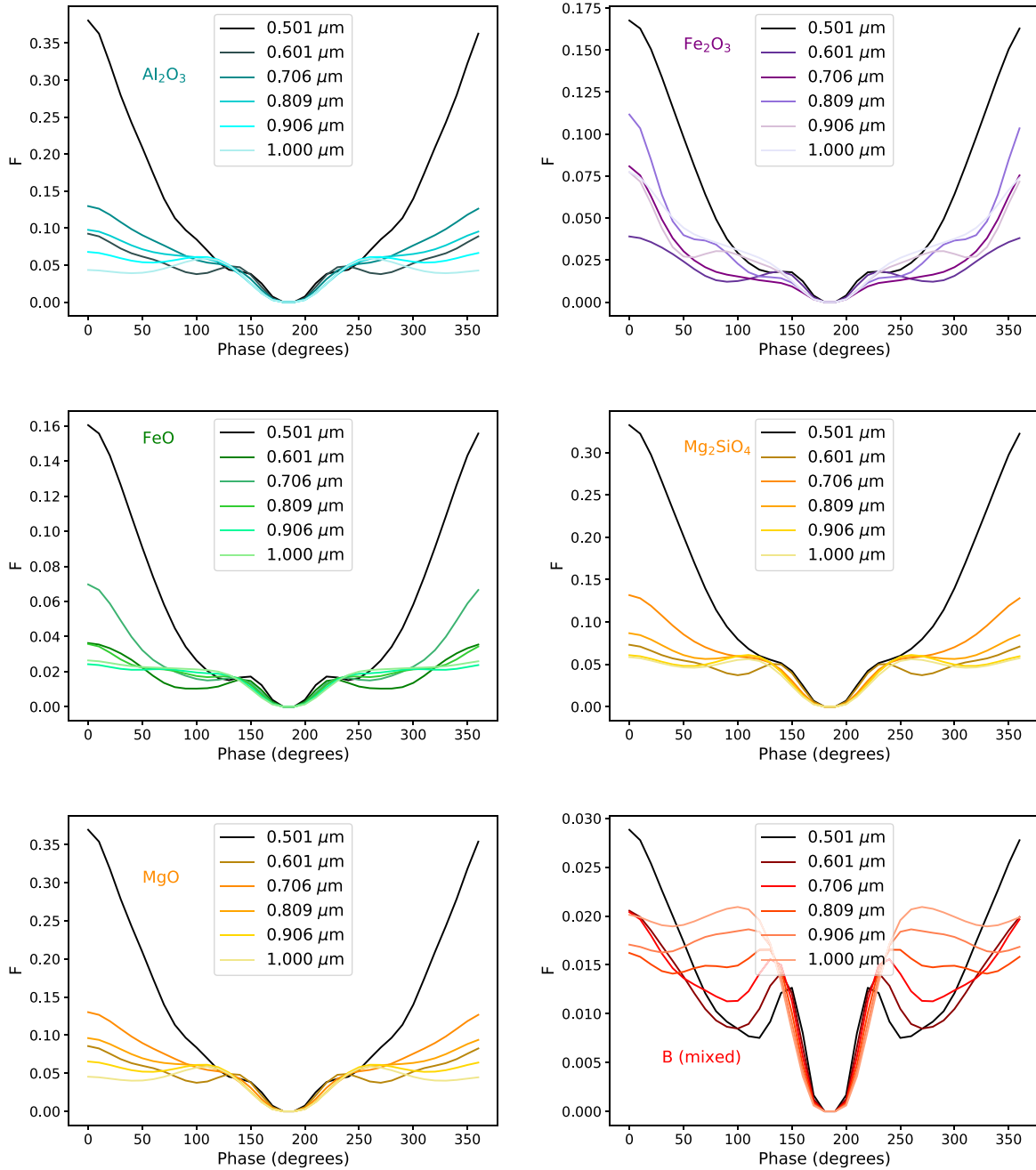
Figure B4. Phase curves for reflected flux *F* for homogeneous planetary atmospheres composed of clouds formed from a single species (as labelled in each panel), and atmosphere type B. The phase curve for the homogeneous planetary atmosphere type B but with mixed species for the clouds is shown in the lower right panel for comparison.
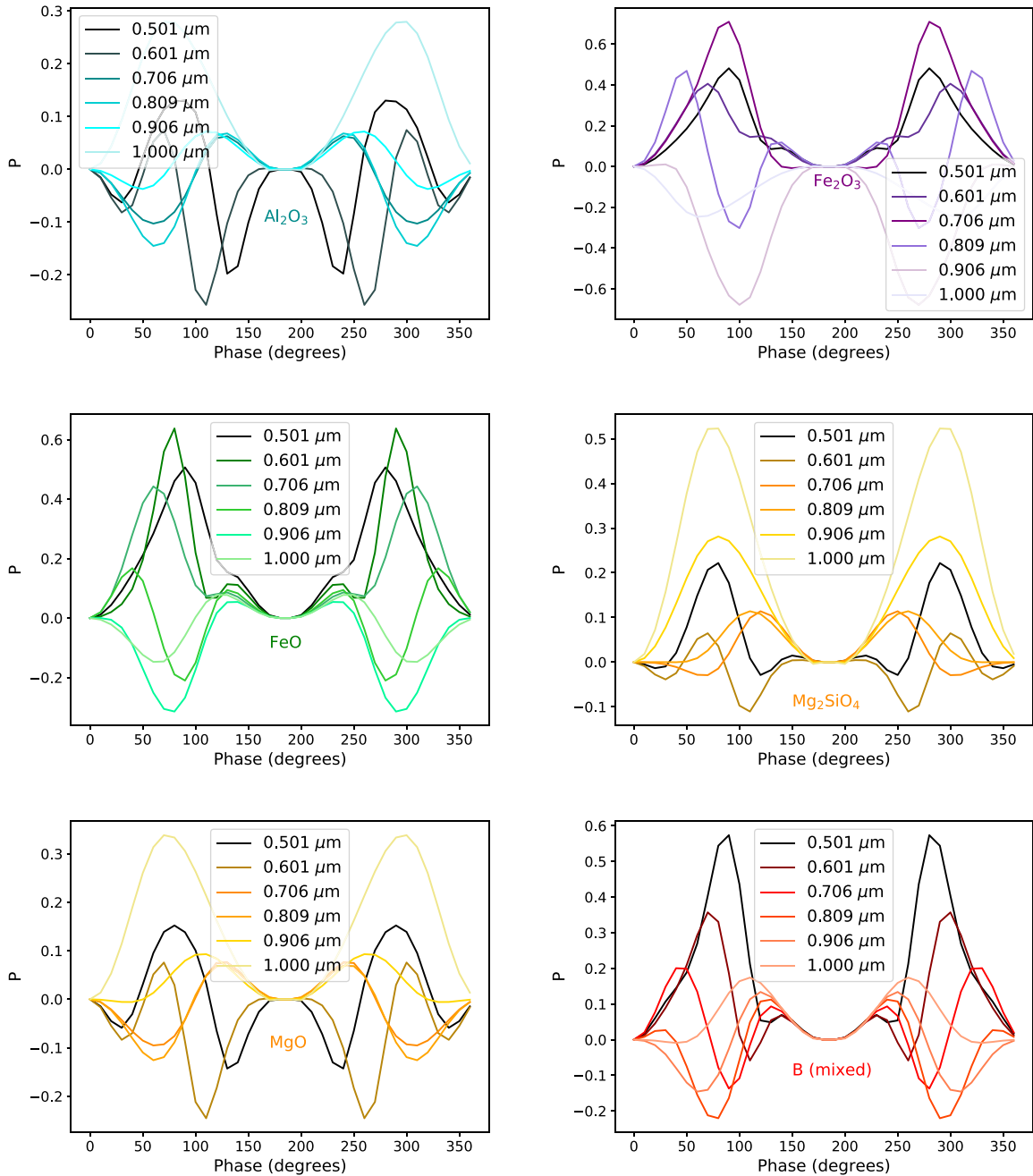
Figure B5. Phase curves for degree of linear Polarization *P* for homogeneous planetary atmospheres composed of clouds formed from a single species (as labelled in each panel), and atmosphere type B. The phase curve for the homogeneous planet composed of atmosphere type B but with mixed species for the clouds is shown in the lower right panel for comparison.
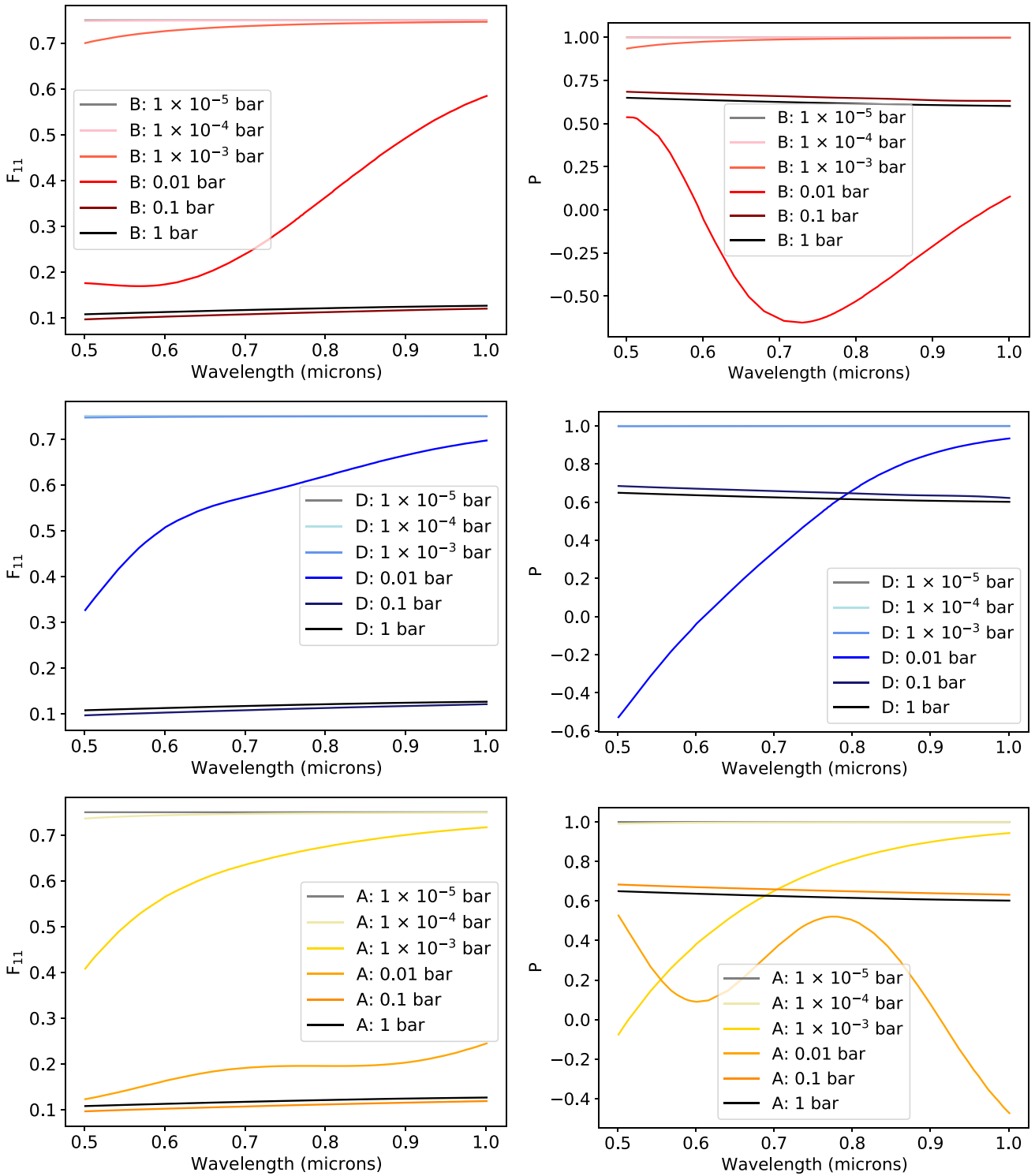
Figure B6. Single scattering matrix elements F_{11} (left panels) and P (right panels) for a scattering angle of $90°$ as a function of wavelength, for the cloud setups used for different pressure layers (as labelled) of atmosphere regions B (upper panels), D (middle panels), and A (lower panels).
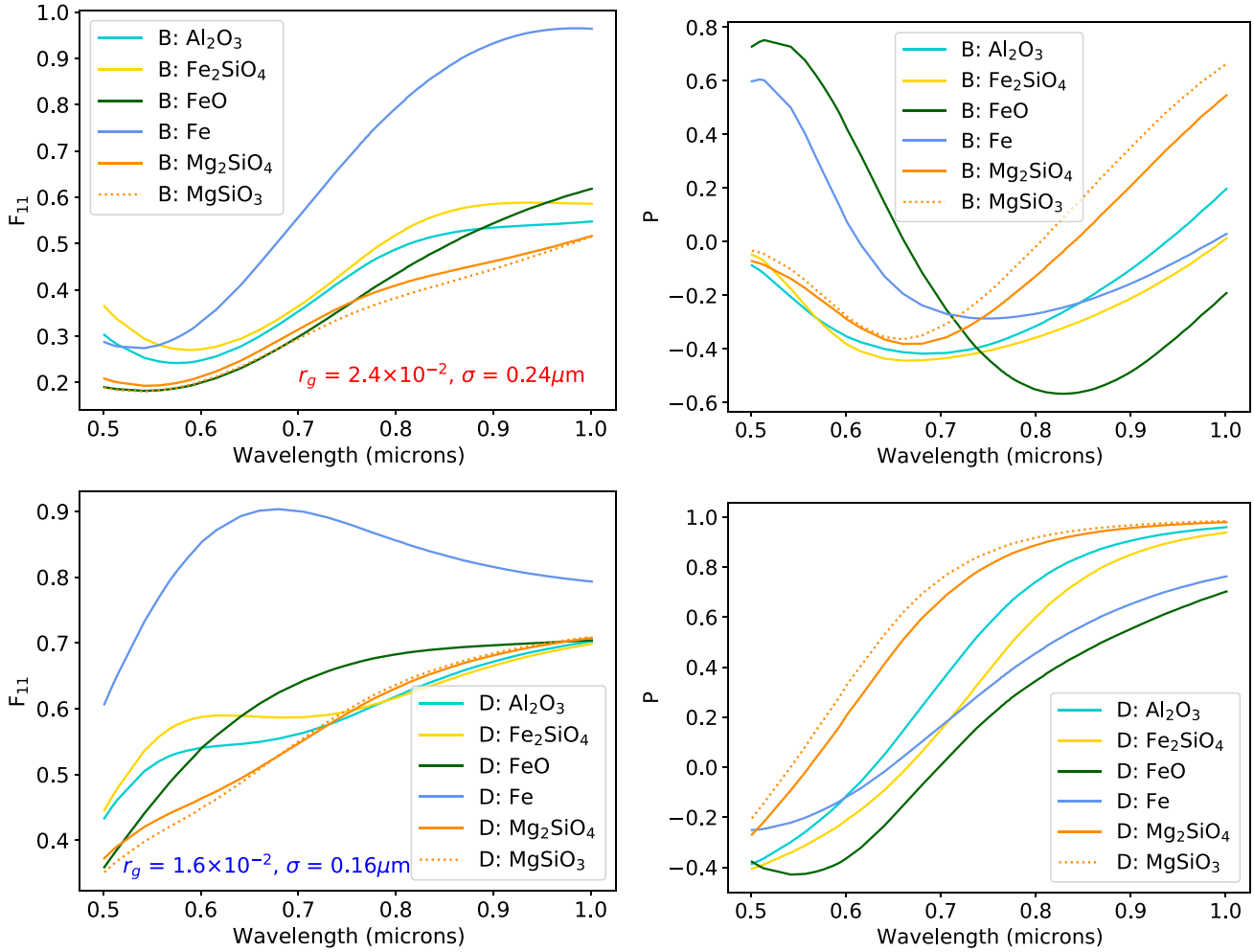
Figure B7. Single scattering matrix elements F_{11} (left panels) and P (right panels) for a scattering angle of $90°$ as a function of wavelength, for various species as labelled. The size distribution from atmosphere type B (upper) at 0.01 bar (2.4×10^{-2} around $0.24\,\mu$m), and for atmosphere type D (lower) at 0.01 bar (1.6×10^{-2} around $0.16\,\mu$m) are compared.

This paper has been typeset from a TEX/LATEX file prepared by the author.